Case Studies in Construction Materials 23 (2025) e05014

Contents lists available at ScienceDirect

Case Studies in Construction Materials

journal homepage: www.elsevier.com/locate/cscm

Carbonation of lightweight alkali-activated aggregates based on biomass fly ash: Effect on microstructure and leaching behavior

Anže Tesovnik [a,b], Lisbeth M. Ottosen [c], Vilma Ducman [a,*]

[a] Laboratory for Cements, Mortars and Ceramics, The Department of Materials, Slovenian National Building and Civil Engineering Institute, Dimičeva ulica 12, Ljubljana 1000, Slovenia
[b] Jožef Stefan International Postgraduate School, Jamova cesta 39, Ljubljana 1000, Slovenia
[c] Department of Environmental and Resource Engineering, Technical University of Denmark, Brovej, Lyngby 2800, Denmark

ARTICLE INFO

Keywords:
Artificial aggregates
Lightweight aggregates
Biomass fly ash
Alkali-activated materials
Carbonatisation
Leaching

ABSTRACT

Artificial aggregates offer a sustainable solution to large-scale waste utilization and the increasing demand for limited natural aggregates. This study extends the understanding of the production of artificial lightweight aggregates with a variable rotation speed approach based solely on biomass fly ash (BFA) alkali-activated materials (AAMs). Systematic variation of alkali content and solution density at a constant water-to-solids ratio showed that alkali concentration significantly influences granulation beyond what can be explained by water availability. The interplay between alkali activation and carbonation was investigated using different mix designs and curing conditions, as well as comparing simultaneous curing carbonation with post-cure carbonation. The results were evaluated with regard to the effects on the macro- and microstructural properties as well as on the leaching behavior. Prolonged carbonation initiated after aggregate formation resulted in premature depletion of Ca, limiting the development of C-A-S-H gels and increasing microporosity, leading to a reduction in mechanical properties. In contrast, post-curing carbonation maintained a compressive strength of over 1 MPa while still allowing carbonation benefits, resulting in compressive strengths comparable to lightweight expanded clay aggregates. Carbonation also proved to be an effective leaching mitigation strategy by stabilizing heavy metals through both physical encapsulation and chemical pH regulation. These results underline the importance of carbonation timing in high Ca AAMs and highlight lightweight aggregates as a viable pathway for BFA valorization, CO_2 sequestration and sustainable construction applications. This approach offers an alternative valorization strategy for BFA facing regulatory restrictions for direct use in cement, while contributing to carbon capture and circular economy initiatives.

1. Introduction

Artificial aggregates present a promising alternative to natural aggregates, offering unique properties and significant potential to enhance the sustainability of the construction industry. Aggregates typically consist of granular materials and are a critical component of concrete and composite materials. The construction sector significantly contributes to greenhouse gas emissions [1], so a circular

Abbreviations: BFA, Biomass fly ash; AAM, Alkali-activated material; AC, Ambient curing; HHC, Heat and humidity curing; CEC, CO_2-enriched curing; PCC, Post-curing carbonation.

* Corresponding author.
E-mail addresses: anze.tesovnik@zag.si (A. Tesovnik), limo@dtu.dk (L.M. Ottosen), vilma.ducman@zag.si (V. Ducman).

https://doi.org/10.1016/j.cscm.2025.e05014
Received 11 April 2025; Received in revised form 20 June 2025; Accepted 3 July 2025
Available online 4 July 2025

economy model utilizing waste and secondary raw materials can be beneficial from both an economic and an environmental point of view [2]. Pressures such as CO_2 emission quotas, waste regulations, the demand for less pollution, and economic efficiency will increasingly challenge the sector. Among the promising approaches to meet such demands is the production of artificial aggregates, which enable the high-volume reuse of waste materials while achieving the desired final properties.

The production of biomass ash, a combustion residue from different types of biomass, has been increasing for years as fossil fuels are being replaced by renewable sources [3,4]. The co-combustion of biomass with coal is employed as a strategy to reduce NO_x and SO_x emissions [5], enhancing the combustion performance [6] and cost efficiency [7]. With approximately 50 Mt of annual biomass ash produced in Europe, 170 Mt/yr globally [8], and as biomass is expected to be the most used alternative to fossil fuels for energy and heat production in Europe [9], it may pose a significant challenge for landfilling, environmental safety, and future waste management. It is hence concerning that only a few valorisation processes have been established for biomass fly ash (BFA). The added economic value to the final products applied for soil alkalinity amendment or fertilizer in the agriculture sector is also limited [10–12].

As the first approach, many recent studies focusing on construction materials suggested the reuse of BFA as a substitute material in cement production [13–18]. However, the relevant standards do not yet accept those practices or their use is limited. The use of ash in construction materials is regulated by EN 197–1 for cement and by EN 450–1 and ASTM C618 for concrete. Currently, these standards primarily address coal fly ash and impose the same strict requirements for alternative ashes, which must meet the hard-to-reach strict chemical, performance, and environmental criteria as coal fly ash. Some current standards, e.g. ASTM C618, specify an exclusive use of coal combustion ash excluding ashes produced by the co-firing of biomass and coal. While these regulations for ash use in cement vary by region and ash type, national standards are often built on international frameworks (e.g. EN or ASTM) and adapted to local materials, environmental regulations, and construction practices, where additional requirements must be met.

A sustainable alternative use for BFA is provided by alkali-activated materials (AAMs), where materials with significant reactive amorphous silica and alumina [19,20] can be utilized as precursors. AAMs are synthesized through a chemical reaction (also referred as "geopolymerization") between amorphous aluminosilicate precursors and alkaline activators, such as sodium silicate or sodium hydroxide, to form an inorganic binder composed of a cross-linked aluminosilicate gel network. Lower energy consumption and potential waste valorization [21–25] provide a low-carbon alternative to conventional cement. Compared to industrial secondary raw materials, like coal fly ash and various types of slags, the research applications of biomass ash in AAMs remain relatively underexplored [26]. Agricultural biomass ashes such as rice husk ash [27,28] or palm oil ash [29,30] have been investigated as precursors for AAMs. Soriano et al. [31] even investigated the production of alternative alkaline activators from agricultural ash, and the results suggest suitability, however the cost-effectiveness is currently questionable. Although biomass ash is frequently considered as a supplementary cementitious material [14–16,18,32], AAMs solely based on biomass ash remain less studied and are usually explored in blended mixtures or as composites with metakaolin [33–36].

A recent growth of research in the field of artificial aggregates [37] focused on different aggregation methods [38,39], where disk pelletization emerged as the most widely used and easily adaptable technique for industrial implementation [40,41]. The most commonly studied materials for pelletization include coal fly ash [42–44] and ground granulated blast-furnace slag (GGBFS) [45,46], although they are directly used as cement additives, making their use in aggregates less favorable or potentially inefficient. A recent review of publications on artificial aggregates [40] showed, cementitious-based artificial aggregates, which bind secondary raw materials using small amounts of cement, to be the most explored type. In contrast, cement-free alkali-activated aggregates are a relatively new area of research that has yet to be comprehensively studied to achieve industrial acceptance.

Besides its suitability in AAMs, BFA has the potential for applications in carbon sequestration. Owing to its reactive minerals rich in Ca and Mg, such larnite, forsterite or portalandite [47], BFA can interact with CO_2 to form stable carbonates. This process mineral carbonatisation can permanently sequester CO_2 and align with net-zero industry goals by lowering atmospheric CO_2 levels. While the number of studies on biomass-based materials and aggregates are growing, some critical gaps in biomass alkali-activated aggregates remain unaddressed. Carbonation can densify the matrix of concrete and AAM products, enhancing their durability and reducing porosity. The carbonation process in AAMs requires further investigation, as results from different precursors might be inconsistent with methodologies applied in carbonation, also resulting in adverse effects. In some cases, carbonation has been shown to reduce the mechanical strength, highlighting the need for a deeper understanding of the underlying mechanisms influencing the overall performance.

Upcycling industrial byproducts into AAMs may increase heavy metal leaching due to an initial pH rise or an inadequate mix design, causing unreacted alkalis and a weakly linked Si network [48]. While the research on leaching in cement-based (OPC) composites is extensive, studies on AAM and its composites remain limited [49]. Sintering can lower leaching in precursors and lightweight aggregates by stabilizing the matrix [50,51]. However, such high-temperature processing is gradually being abandoned due to carbon emission requirements. Instead, cold-bonding techniques should be explored in other sustainable leaching mitigation approaches. Lancelloti et al. explored the chemical stability of geopolymers municipal solid waste incinerator fly ash to reduce pollutant mobility [52], where a proper mix design is essential to achieve a stable product. Additionally, the carbonation and hydration of wood ash have been shown to lower heavy metal leaching by forming stable phases [53]. The combined effects of AAM aggregate carbonation on the leaching behavior and physical properties remain unexplored.

This study enhances the understanding of aggregation parameters in AAMs solely based on biomass BFA. It also addresses the ambiguous effects of water and alkali content on the pelletization efficiency of AAM aggregates. Some studies identified activator molarity as the most critical factor for pelletization efficiency [54], while others argue that pellet formation only depends on the water content, with the alkali content being irrelevant [55]. Most studies focus on hydroxide activators, whereas silicate solutions like Na_2SiO_3 not only provide alkalinity but also supply additional silica for the AAM formation. Despite their higher viscosity, the role of silicate activators in granulation remains largely unexplored for AAM aggregates. To address this gap, our study investigates the

influence of silicate solution and water content on pelletization by maintaining a fixed water-to-solid ratio, calculated based on bulk water content to isolate the effects of alkali content and solution density on the pelletization efficiency of the AAM aggregates.

Unlike conventional disc pelletization, typically carried out at a uniform lower rotational speed, this study introduces a novel variable-speed pelletization approach to ensure high pelletization efficiency while enhancing a lightweight, porous structure optimized for rapid carbonation applications. The dual effect of alkali activation and carbonation in producing artificial aggregates solely from BFA was investigated, focusing on mechanical properties, microstructural evolution, the chemistry of AAM matrix development, and the heavy metal leaching behavior.

A key aspect is the systematic comparison of different curing conditions, particularly the role of carbonation effects with respect to timing and reaction mechanisms, where both accelerated carbonation during aggregate formation and post-curing carbonation were examined from macro- to microstructural levels. By distinguishing between these approaches, the study explores the critical balance required to optimize the synergy between alkali activation and carbonation. Additionally, it highlights the potential of lightweight aggregates as an efficient medium for rapid carbonation and positions artificial aggregate production as a promising pathway for BFA large-scale valorization, expanding application possibilities for this underutilized industrial byproduct.

2. Materials and methods

2.1. Characterisation of biomass fly ash (BFA)

The BFA was sourced from a local heat and power plant, where ash is a main byproduct from the co-combustion of brown coal with approximately 15 % wood chips. The plant produces around 6000 tons of ash annually. The ash was sieved to obtain particles below 400 μm (Fig. 1a), eliminating larger debris and improving the granulation (i.e., pelletization) efficiency by increasing the favorable proportion of fine particles. The size of the pre-sieving was also chosen from a practical and industry-acceptable approach, offering a fast, low-energy solution that aligns with the valorization potential and scalability requirements of industrial applications.

The particle size distribution (PSD) of the BFA was determined using laser diffraction granulometry (Microtrac MRB Sync+TurboSync laser grain size analyzer, PA, USA). Samples were measured in the isopropanol dispersion mode with applied sonication to achieve a uniform suspension, prevent agglomeration and improve the measurement accuracy. Scanning electron microscopy (SEM; Jeol JSM-IT500, Japan) was performed on an unpolished BFA powder sample under low vacuum conditions to observe particle morphologies and size distributions. The PSD presented in Fig. 1b shows a bimodal distribution typical of BFA, with major peaks at approximate diameters of 20 and 205 μm, where the first peak in the fine particle region indicates the presence of smaller spherical particles and a secondary peak of larger particles predominantly representing incompletely combusted material of irregular shapes as can be observed in the SEM micrograph in Fig. 1c. The cumulative distribution curve confirms that 50 % of the particles (d50) fall below a diameter of 47 μm.

The chemical composition of BFA was determined by X-ray fluorescence (XRF) spectroscopy and is presented in Table 1. The sample was milled (Siebtechnik vibrating disk mill), sieved to < 63 μm, and ignited at 950 °C for 2 h to measure the loss on ignition ($LOI_{950\ °C}$). To prepare XRF discs, the sample was combined with a Li-tetraborate and Li-metaborate flux mixture (1:10 wt ratio, Fluxana FX-X50–2) and LiBr solution (7.5 g in 50 ml H_2O, Acros Organics) as a non-sticking agent. The mixture was melted in platinum crucibles, and discs were analyzed using a Thermo Scientific ARL Perform'X Sequential XRF (Thermo Fisher, MA, USA) spectrometer with the UniQuant 5 software.

The mineralogical characteristics of the BFA were determined using X-ray diffraction (XRD, Empyrean PANalytical, Netherlands) with CuKα$_1$ radiation ($\lambda = 1.54$ Å). Measurements were taken over a 4–70° 2θ range with a step size of 0.0263°. The powder sample was back-loaded into a cylindrical holder to avoid the preferred orientation. The diffraction patterns were evaluated by Rietveld refinement using PANalytical X'Pert HighScore Plus software v. 4.8, and the amorphous phase was quantified using an external Al_2O_3 (NIST676a, corundum) standard. The XRD pattern of BFA exhibits a pronounced halo, indicating a notable amorphous phase content of 45.8 % (Fig. 2). The detailed mineral phases, their corresponding chemical formulas, and reference codes are listed in

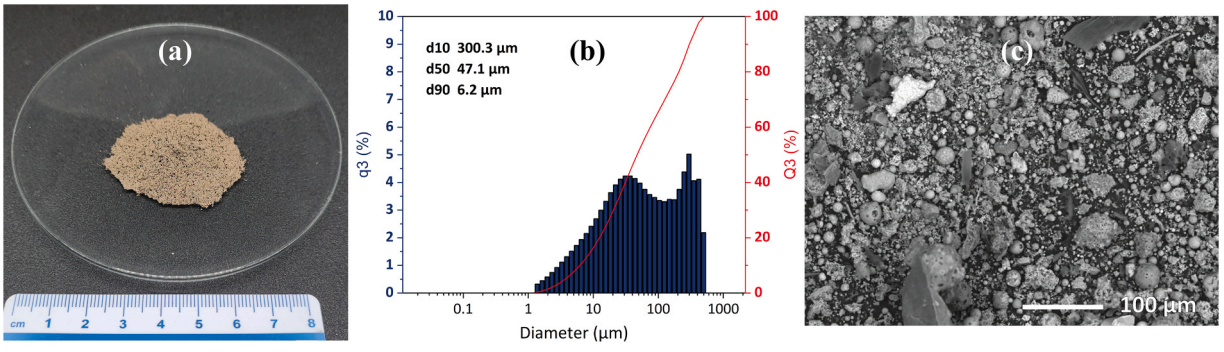

Fig. 1. (a) Fine BFA sieved below 400 μm. (b) PSD of sieved BFA presented as a differential distribution q3 and cumulative distribution Q3. (c) SEM micrograph of sieved BFA at the magnification of x 250.

Table 1
Chemical composition of BFA used in the study according to XRF.

SiO_2 (wt%)	Al_2O_3 (wt%)	Fe_2O_3 (wt%)	CaO (wt%)	MgO (wt%)	Na_2O (wt%)	K_2O (wt%)	SO_3 (wt%)	MnO (wt%)	P_2O_5 (wt%)	TiO_2 (wt%)	$LOI_{950\ °C}$ (%)
27.19	10.80	11.95	19.67	7.88	0.39	2.12	1.26	0.25	0.60	0.53	16.89

Supplementary Table S1.

The content of elements in the amorphous phase potentially available for alkali activation, was calculated by subtracting the elements in the crystalline content (XRD data) from the elements in the overall composition (XRF data), according to the procedure in the previous research [56]. The important elements likely contributing to an alkali activation of BFA are shown in Fig. 3, where their distribution in the mostly non-reactive crystalline and significantly more reactive amorphous phases is presented. A significant amount of Si and Al in the amorphous phase shows the suitability of this BFA as a precursor for alkali-activated applications.

Additionally, the significant presence of Ca might enhance the development of structural matrices in AAMs, promoting the formation of calcium silicate hydrates and calcium aluminate silicate hydrates [57]. Moreover, Ca exhibits a dual functionality in AAM systems, by potentially contributing to CO_2 sequestration through mineral carbonation. Nilsen and Quaghebeur [47] highlighted the reaction between dissolved CO_2 and alkaline phases, where, crystalline Ca-bearing mineral phases such as lime can be susceptible to carbonatization in addition to dissolved Ca.

Fourier Transform Infrared spectroscopy (FTIR; PerkinElmer Spectrum Two, MA, USA) was performed with an attenuated total reflection accessory (ATR mode, diamond/ZnSe crystal) in the range of 380–4000 cm^{-1} on BFA to identify the presence of chemical bonds and functional groups, providing insights into the structure and indicating reactivity of precursor. The FTIR spectrum of the BFA precursor with additional explanations is provided as Supplementary Figure S1, the spectrum aligns with the chemical and mineralogical composition of the precursor.

2.2. Mixture design and granulation

Three different mixtures were prepared to evaluate the influence of alkali and bulk water content on the granulation efficiency and mechanical properties of the artificial aggregates prepared from BFA.

Two alkali-activated mixtures were target-optimized by adjusting the amounts of BFA and sodium silicate activator (Na_2SiO_3; Geosil 34417, Wöllner, Germany; SiO_2 27.5 m%, Na_2O 16.9 m%, H_2O 55.6 m%) to achieve the specific theoretical elemental ratios between alkali metals (e.g., Na, K) and the Si and Al in the mixture (Table S2 in the Supplementary Material). A third mixture was prepared as a control sample, consisting solely of ash mixed with distilled water. The density of the solutions was measured by a density meter (Anton Paar Germany Gmb, DMA 35 Standard, Germany). The water-to-solid ratio was determined by trial and error, and the fixed value of 0.5 was found to be optimal, where the ratio takes into account the sum of the water from the sodium silicate solution and the added distilled water. Table 2 presents the mix design where the only varying parameter was the alkali content. The water-to-solid ratio for the BFA pelletization is higher than the typical 0.3 used for fly ash [58] due to the presence of non-combustible wood particles and cellulose, which increase the water demand [59].

The artificial aggregates were produced using a disc pelletizer (EIRICH TR04 Disc Pelletizer, Germany) with a 40 cm diameter and a 45° pan angle. Unlike conventional disc pelletization, which is typically performed at a constant lower rotational speed [60], an unconventional two-step approach with a variable rotation speed was used to optimize pelletization efficiency while maintaining a high porosity suitable for carbonation applications. The process parameters were determined through trial and error to identify the

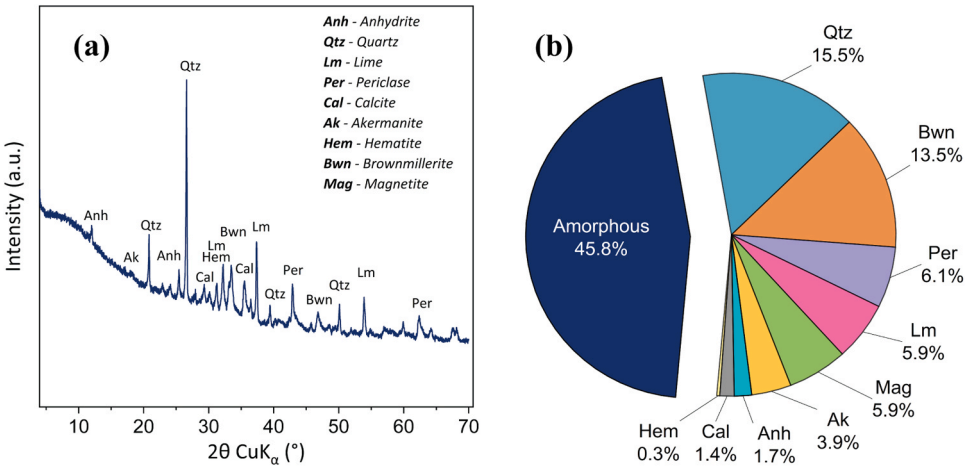

Fig. 2. (a) XRD pattern of BFA used in the study, (b) and identified mineral phases with their corresponding percentage.

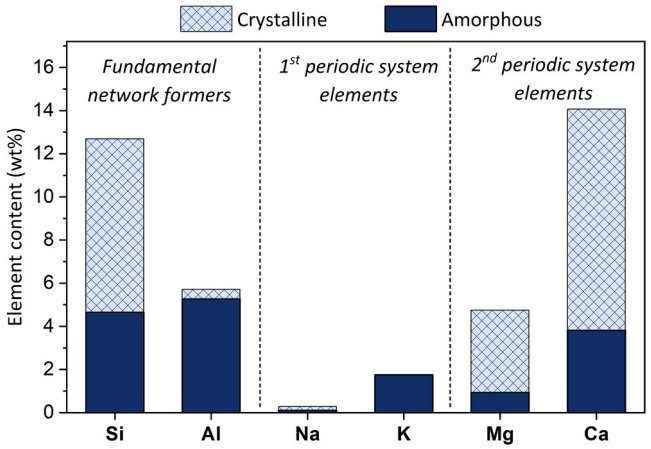

Fig. 3. wt% distribution of elements in BFA, indicating elements potentially participating in alkali activation within the reactive amorphous phase and those present in the non-reactive crystalline phases.

Table 2
Mix design of artificial aggregates produced from BFA, including calculated bulk water consumption, water-to-solid ratio, and pelletization efficiency.

Mixture	BFA [g]	Na_2SiO_3 solution [g]	Additional H_20 [g]	Bulk H_2O [g]	H_20/solid /
M1	250	112	63	125	0.5
M2	250	80	80.5	125	0.5
M3	250	0	125	125	0.5

optimal setup for BFA that ensures efficient pelletization while preserving the desired lightweight structure. Initially, the disc was rotated at 45 rpm, and half of the alkaline solution was evenly sprayed over the BFA surface to form numerous nuclei during the first 2 min. The disc speed was then increased to 130 rpm, and the remaining solution was sprayed in two equal intervals over the next 4 min. The process was finalized by an additional 2 min of rotation without adding further solution.

The pelletization efficiency of the artificial aggregates was calculated as the proportion of the mass ratio of the produced aggregates bigger than 4 mm to the total mass of the batch.

2.3. Curing and carbonation conditions

The artificial aggregates were subjected to three curing regimes for 28 days to study the effect of the curing conditions on the mechanical and chemical properties of the artificial aggregates:

- Ambient Curing (**AC**): at constant conditions of 20°C and 55 % relative humidity (RH),
- elevated Heat and Humidity Curing (**HHC**): in a controlled chamber set to 40°C and 80 % RH to simulate accelerated curing conditions,
- CO_2-Enriched Curing (**CEC**): in a controlled chamber at 40°C and 80 % RH with an increased CO_2 concentration of 4 vol%, aiming to enhance carbonation processes during curing.

Alkali-activated aggregates following the M1 mix design (Table 2), with the higher alkali content, additionally underwent a Post-Curing Carbonation (**PCC**). Aggregates were first cured under elevated temperature and humidity conditions (40°C, 80 % RH) for 14 days and then exposed to an enriched CO_2 environment (40°C, 80 % RH, 4 vol% CO_2) at the same temperature and humidity for an additional 14 days. This postponed accelerated carbonation process was designed to assess the importance of carbonation timing.

2.4. Characterisation of the alkali-activated aggregates

Compressive force measurements were performed for each mixture formulation and curing regime at intervals of 3, 7, 14, and 28 days to evaluate the influence of mix design and curing conditions on the development of the mechanical properties. A mechanical-strength testing machine (ToniTechnik ToniNORM, Berlin, Germany) was used for the compressive force test, conducted on 20 aggregates with spheric geometry in the size range of 8–11 mm. The diameter of the spherical samples was measured using a digital vernier caliper (Digital ABS AOS Caliper, accuracy: ± 0.02 mm). The compressive strength (CS) was calculated using the following formula:

$$CS = \frac{CF * 2.8}{\pi * d^2} \quad (1)$$

Where CF is measured compressive force load (N), and d is the diameter of spherical aggregates (mm). The equation normalizes compressive strength by diameter, accounting for size effects and ensuring comparability across aggregates of different dimensions [61].

The bulk density of the artificial aggregates was determined according to CEN EN 1097–3:1998 [62], following the procedure for lightweight aggregates. The skeletal density was determined using mercury intrusion porosimetry (MIP; Micromeritics Autopore IV 9500 porosimeter, GA, USA), which was also used to determine the pore size distribution and total porosity. Measurements were performed on samples cured for 28 days, which were dried to a constant mass, using at least three representative aggregates per mix and curing treatment to ensure representative results.

To evaluate the influence of the alkali activator content, curing conditions, and carbonation on chemical and mineralogical changes, aggregates cured for 28 days and obtained from the compressive force measurements were crushed and then milled using a vibrating disk mill, sieved to a particle size below 63 μm and analyzed using XRD and FTIR to detect changes in mineralogy and chemical structure.

Thermogravimetric analysis (TGA) was performed to assess the effect of carbonation on artificial aggregates after 28 days of curing. The analysis of crushed and sieved (<63 μm) aggregate samples was carried out using a STA 409 PC Luxx Simultaneous Thermal Analyzer (Netzsch-Gerätebau GmbH, Selb/Bayern, Germany). Samples were heated from 25 to 900°C at a rate of 10 K min^{-1} , with a continuous N_2 flow of 20 ml min^{-1} to prevent oxidation.

Polished cross-sections of artificial aggregates embedded in epoxy resin (Bluehler EpoThin 2, IL, USA) were examined by scanning electron microscope (SEM; Jeol JSM-IT500, Japan) equipped with an energy dispersive X-ray spectrometer (EDXS; Oxford Instruments, UK) with a W-filament, under low-vacuum conditions using an accelerating voltage of 15 kV to study the reacted precursor, AAM matrix, microstructure and distribution of the phases, as well as the observation of carbonation. Semi-quantitative chemical composition was evaluated by EDXS elemental mapping and point analysis using AZtec software v. 5. To assess the effects of carbonation and compositional variations within the AAM matrix, multi-point EDXS analysis was conducted on non-carbonated and carbonated samples at 450 × magnification to capture a broader spatial distribution, thereby reducing the influence of material heterogeneity and providing a more representative global composition. In total, more than 150 measurement points for each cross-section were manually distributed over the reacted AAM matrix to obtain statistically significant elemental data.

The methodology following SIST EN 12457-4:2004 [63] was applied to assess the leaching behavior of the BFA and AAM aggregates. Crushed samples were suspended in distilled water at a liquid-to-solid ratio of 10 ml/g and stirred at 10 rpm for 24 h. The pH of the suspensions was measured, and the solutions were subsequently filtered. The concentrations of As, Cr, Cu, Mn, Mo, Ni, and Pb were analyzed using inductively coupled plasma optical emission spectroscopy (ICP-OES; Varian 720-ES, USA). Each leaching test was conducted in triplicate, with results reported as mean values with standard deviations.

3. Results and discussion

3.1. Variable-speed pelletization and the effect of activator solution

The effects of variable-speed pelletization on aggregate formation and properties were investigated. At the initial lower rotation speeds (45 rpm) of the disc pelletizer, liquid bridges form between the precursor particles [38], where surface tension force promotes nucleation. In the second step, a higher applied rotational speed (130 rpm) generated greater shear forces, preventing excessive compaction while maintaining an open, porous structure that still supported growth without nucleus breakdown (Fig. 4). The rapid particle movement at a higher speed increased the likelihood of temporary void formation and air entrainment, enhancing pore interconnectivity. By first forming stable nuclei at a lower speed and then accelerating the rotation, aggregate growth was controlled to promote structured porosity rather than uncontrolled densification. In comparison, Ferraro et al. [64] produced lightweight aggregates

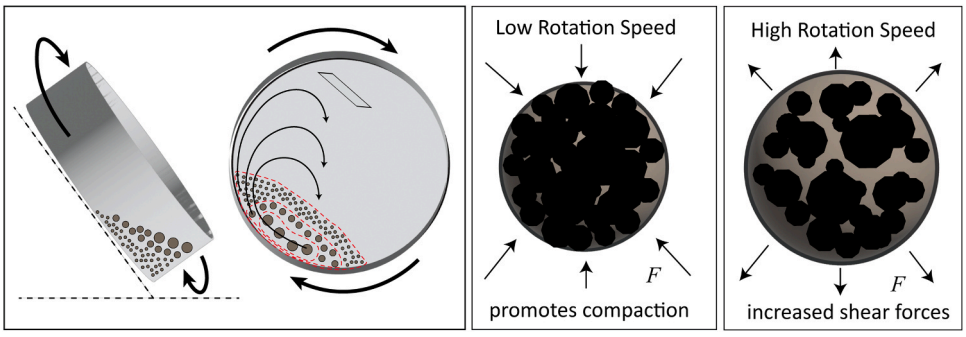

Fig. 4. Schematic representation of the disc pelletization process, illustrating the effect of rotational speed and applied forces on aggregate formation.

from municipal solid waste incineration fly ash bound with a low addition of OPC and a uniform rotation speed, where MIP detected a total porosity of approximately 35 %. The non-conventional BFA pelletization approach, utilizing a dual-step rotational speed approach, achieved the notable pelletization efficiency (Table 3) while maintaining a high porosity of 45–59 % in AAM aggregates (3.3. Microstructural Analysis, Fig. 5).

Pelletization efficiency was highest in M1 (78 %), followed by a similar value in M2, while the water-only mixture (M3) exhibited a significantly lower efficiency (62 %), as stated in Table 3. Although the pelletization efficiency is influenced by multiple factors, including precursor properties, the pelletization process and the characteristics of the alkaline activator solution [40], some studies of AAM aggregates using NaOH activators suggest that pellet formation is solely dependent on water content only, with alkali content playing no significant role [55]. The presented results using Na_2SiO_3 indicate that AAM aggregates (M1 and M2) achieved a higher efficiency than M3, despite all mixtures maintaining a fixed w/s ratio of 0.5, the same precursor, and identical pelletization conditions. This suggests that water alone is not the sole determinant of pelletization efficiency in silicate solution AAM aggregates. The density of the solution, stated in Table 2, likely influenced the initial stage of pelletization, where the sprayed solution forms a liquid bridge between precursor particles, mechanically binding them together. Liquids with higher density often exhibit increased surface tension and viscosity due to stronger intermolecular interactions and cohesive energies [65]. Silicate-rich solutions (e.g., Na_2SiO_3) have a higher density than water or hydroxide solutions (e.g., NaOH), which enhances their ability to promote effective pellet formation. However, optimal solution parameters are required to balance workability and performance. Insufficient surface tension leads to over-wetting, resulting in poor granule cohesion or collapse, whereas higher surface tension improves pellet integrity by maintaining a stable shape. Excessively high density and viscosity might hinder spreading on solid surfaces, reducing wetting efficiency and limiting uniform spray deposition. Furthermore, the alkali content and pH in the solution may also influence the early-stage alkali activation process, as initial reactions could already begin within the 8-minute pelletization period.

These findings are particularly relevant for one-part alkali-activated aggregate systems (so-called "just add water" AAMs), where solid activators are pre-mixed with the precursor and activated upon water addition [66], especially if solid-state anhydrous silicates are used. Understanding the role of alkali content and activator solution in the granulation process is essential to achieving the desired high production efficiency.

3.2. Physical and mechanical properties

The mixtures M1–3 were subsequently cured under three different curing conditions to evaluate their physical and mechanical properties.

The compressive strength development of artificial aggregates subjected to different curing regimes is presented in Fig. 5. A comparative examination of mix designs revealed that M1, with the highest alkali activator content and a Si/Al molar ratio of 1.9 (Table S2 in the Supplementary Material), consistently exhibited the highest compressive strengths across all curing conditions and time development measurements. This optimized mixture M1 demonstrated both lightweight properties (bulk density up to 1.5 g/ml) and superior compressive strengths, possibly exceeding 1 MPa with temperature curing, which is comparable to the mechanical performance of lightweight expanded clay aggregates. Unlike the latter, which requires high-temperature processing above 1000°C, AAM aggregates can be produced at significantly lower temperatures, offering potential reductions in energy consumption and environmental impact. The results are consistent with the findings of the mechanical modeling of AAMs done by Duxson et al. [67], where the Si/Al ratio close to 1.9 resulted in a maximized compressive strength. The high strength with an optimal Si/Al ratio has been reported to be the result of alumosilicate gel formation, rather than zeolites or silicate derivatives [68]. Mix design M2 (Si/Al = 1.6, lower alkali content) demonstrated up to ca. 78 % lower strength compared to M1 under HHC curing conditions (M1-HCC). In contrast, the M3 control mixture resulted in the lowest compressive strength.

The lack of external thermal or humidity conditions in aggregates subjected to ambient curing (samples M1-AC, M2-AC, M3-AC) resulted in weaker binding and the lowest compressive strengths.

The alkali-activated aggregates cured under heat and humidity conditions (M1-HHC, M2-HHC) exhibited the most significant increase in compressive strength over 28 days (Fig. 5a,b), owing to enhanced reaction kinetics and stronger binding of BFA particles. Previous research on slag-based AAM systems [69] with precursors containing an even higher Ca content showed an almost linear trend between curing time, temperature, and compressive strengths. Here, samples cured at 70 °C exhibited comparable strengths at 3 days to those cured at room temperature for 28 days. In contrast, the HHC aggregates in this study were not only exposed to elevated temperatures but also to a high-humidity environment.

Alkali-activated aggregates cured in CO_2-enriched conditions (M1-CEC, M2-CEC) displayed a non-linear trend in compressive strength. A reduction was observed after 7 days, likely due to interference between early carbonation and the alkali activation process. However, strength increased after 14 and 28 days, indicating a stabilization of the carbonation products and the further development

Table 3
The amount of water and alkali in the solution used for artificial aggregate production, along with the calculated pelletization efficiency.

Mixtures	Bulk amount of H_2O in solution (g)	Amount of alkali (Na_2O) from activator (g)	Density of the alkaline solution (g/cm^3)	Pelletization efficiency (%)
M1	125	18.93	1.314 $_{(17.4\ °C)}$	78
M2	125	13.52	1.234 $_{(17.3\ °C)}$	75
M3	125	0	0.999 $_{(17.6\ °C)}$	62

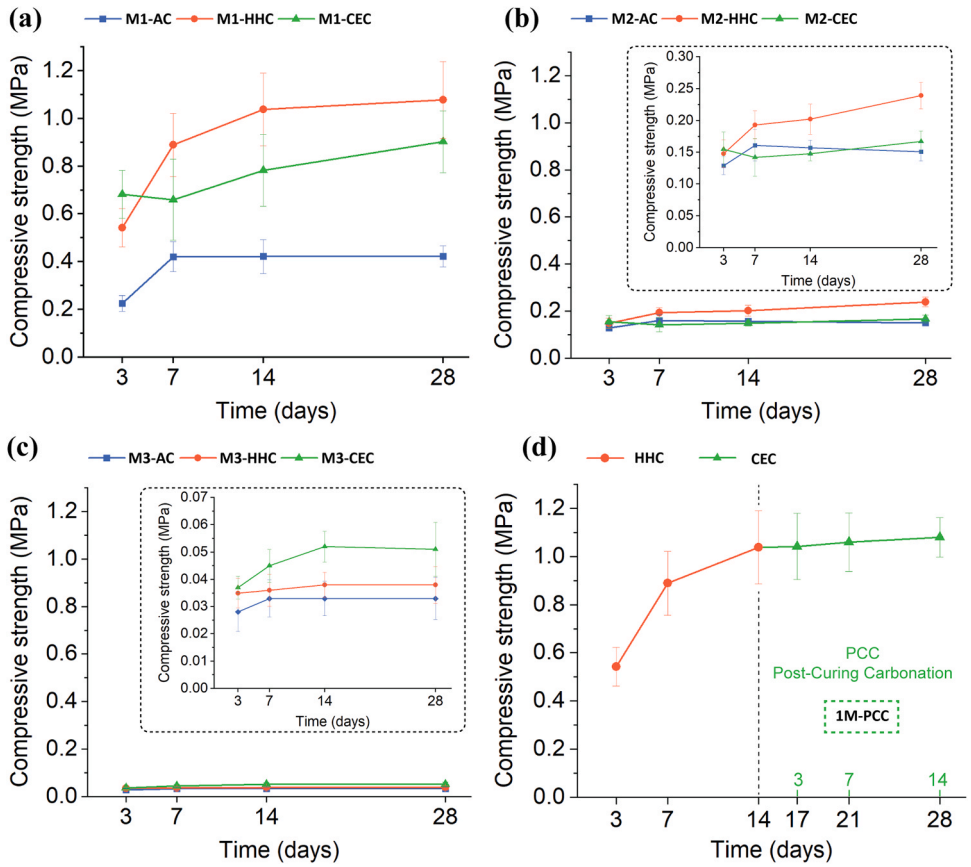

Fig. 5. Compressive strength development under AC, HHC, and CEC conditions for (a) M1 (highest alkali content), (b) M2 (lower alkali content), and (c) M3 (water only). (d) Compressive strength of M1 after post-curing carbonation (PCC).

of binding phases. Control aggregates formed solely with water (no alkali activator) displayed the linearly increasing trend, where the highest compressive strengths under CEC (Fig. 3c, M3-CEC) suggest that carbonation products provided a slight improvement in structural stability. Nonetheless, these compressive strengths remained significantly lower compared to alkali-activated aggregates.

After 14 days of HCC, the aggregates M1-HCC achieved a relative plateau of 96 % of the final strength, subjected to CO_2-enriched conditions for an additional 14 days to undergo post-curing carbonation (Fig. 5d). The final 28-day strength of 1M-PCC aggregates was comparable to that of the 1M-HHC aggregates, indicating that post-curing carbonation neither compromised the structural stability nor significantly enhanced the compressive strength. The comparative graphs of compressive strength development of the same mixture under different curing regimes are presented in Fig. S3 in the Supplementary Material.

Selected physical properties of alkali-activated aggregates with higher alkali content M1 from BFA under different curing regimes are summarized in Table 4. Water absorption was highest for M1-CEC (24.3 %), indicating an increased open porosity, and lowest for M1-HHC (21.5 %), respectively reflecting a lower open porosity. The high values indicate a high proportion of effective porosity, i.e., interconnected void spaces that facilitate fluid transport. M1-AC shows low densities, while M1-HCC showed the densest aggregates. Carbonation introduces different effects, with M1-CEC exhibiting a moderate bulk porosity, likely due to carbonation-induced competition with the alkali activation. In contrast, M1-PCC shows a higher bulk density while maintaining a similar skeletal density, probably influenced by the formation of dense carbonate phases after the majority of the AAM matrix was formed.

The formed aggregates exhibit structural stability, with M1-HHC, M1-CEC and M1-PCC achieving compressive strengths above

Table 4
Selected physical properties of alkali-activated aggregates with a higher alkali content.

Sample	28 d Compressive strength (MPa)	Water absorption (%)	Bulk density (g/cm^3)	Skeletal density (g/cm^3)
M1-AC	0.42	23.48	0.851	1.905
M1-HHC	1.08	21.53	1.539	2.358
M1-CEC	0.90	24.31	1.121	2.022
M1-PCC	1.07	23.21	1.384	2.137

1 MPa, comparable to commercially available lightweight expanded clay aggregates (LECA), where lightweight aggregates complying with EN 13055-1 in fraction 4–10 mm have crush resistance 1.07 N/mm^2 [70]. Zukri et al. [71] reported that sintered clay aggregates with a diameter of 10–20 mm have a strength of 0.8 MPa, although their production requires high-temperature treatment at over 1200 °C. Other lightweight aggregates, such as expanded perlite and vermiculite, which also require high thermal processing, generally have even lower compressive strengths, often below 1 MPa. These materials are usually embedded within a binder matrix in their final applications. For example, perlite-based insulating concrete or plasters must achieve a minimum compressive strength of 0.86 MPa, according to the Florida Building Code [72].

Aggregates with low compressive strengths (below 3 MPa) and high porosity, such as AAM aggregates from BFA, are suitable for non-load-bearing construction elements. Common applications include lightweight concrete, partition walls, insulation layers, and roofing fills, where the main requirements are low density and structural stability, with potential added value provided by properties such as thermal or acoustic insulation rather than high load-bearing capacity. A compressive strength of approximately 1 MPa is sufficient to ensure that the material can support its own weight, withstand handling and minor impacts and sustain any overlay or finishing layers. Furthermore, in our previous research [73], the aggregates with similar strengths (~1 MPa) were embedded in lightweight concrete mixtures, achieving concrete compressive strengths of 17.1 MPa and tensile strengths of 2.8 MPa after 28 days of curing.

3.3. Microstructural analysis

The MIP results presented in Fig. 6 show a change in pore size distribution and total porosity observed after the curing of artificial aggregates. The disc aggregation process involves the liquid agitation of particles through liquid bridge formation and flocculation [38]. As a result, produced artificial AAM aggregates have a larger main pore diameter (with a primary peak around 15 μm) and higher total porosity compared to casted AAM, where particle wetting is higher. The findings are also similar to the OPC cement aggregates, where it has been found that disc aggregation resulted in a lower density and higher porosity compared to the aggregate produced from the same mixture after casting and crushing to produce irregularly formed aggregates [73].

The introduction of a variable rotation speed during pelletization enabled better control over the dynamics of pellet formation dynamics and resulted in aggregates with notably higher open porosity of over 45 % (Fig. 6b) compared to the aggregates described in the literature, which were produced at uniform speed. For example, Masłoń et al. [74] used a slow, constant rotation speed of 30 rpm at 40° to produce coarse aggregates with a fraction of mainly 8 mm of MSWI ash and sediments and achieved an open porosity between 16.8–22.6 %. Ferraro et al. [64] used a fixed speed of 45 rpm at the same inclination with OPC-blended materials and produced coarse aggregates with an open porosity of 20–26 %. For lightweight fly ash AAM aggregates, Risdanareni et al. [75] reported porosity values of 19–35 % at formed at 60 rpm and 48°, while Rudić et al. [41] observed 26–35 % at 45 rpm and 39°. While optimized variable-speed pelletization can improve porosity, industrial- scale application also needs to consider pelletisation efficiency, which is often overlooked in existing studies, although it is important for the process sustainability and upcycling.

Additionally, the curing process played a crucial role in microstructural densification and compressive strength development. For alkali-activated aggregates, the results demonstrate that the curing temperature and humidity significantly influence the pore structure, affecting the microstructure and mechanical properties as described in Section 3.1. The M1-HHC and M2-HCC samples exhibited a reduced total porosity compared to their AC aggregates counterparts, attributed to accelerated reaction kinetics and the formation of a denser matrix (binder formation decreased pores).

With carbonation, the pore diameter of the main peak decreased from 15.7 μm (1M-HHC, same T, RH%, no additional CO_2) to 12.5 μm (1M-CEC) (Fig. 5a). Additionally, a new peak of very fine pores (≈0.003 μm) appeared, along with an increase in total porosity, suggesting potential microstructural deterioration and changes in the binder's integrity. For M1-PCC, the reduction in the main pore

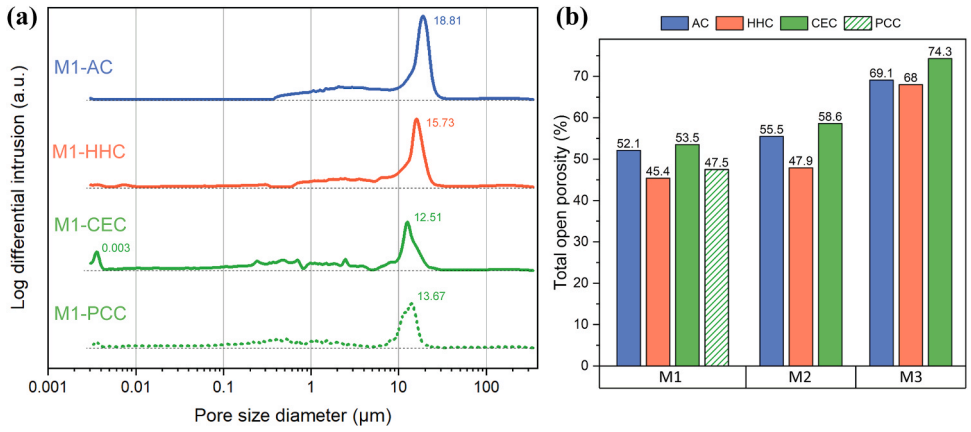

Fig. 6. (a) Pore size distribution in artificial aggregates with the higher alkali content (M1) highlighting the main pore diameters. (b) Total porosity of the produced artificial aggregates treated with the respective different curing regimes.

diameter was less pronounced (13.67 μm). The total porosity increased slightly by + 2 %, indicating a minimal effect on alkali-activated binder formation, as can also be observed in the compressive strength trend in Fig. 3d.

The porosity of the control aggregate M3-HHC was similar to M3-AC. The compressive strengths in this group remained minimal, reflecting the limited binding effect of the newly formed phases. When high-Ca BFA with pozzolanic activity was mixed with water and cured at elevated temperature and humidity, the reaction led to the formation of a weak binding matrix with marginal strength development, primarily driven by the partial hydration of reactive phases and formation of calcium silicate hydrate phases (C-S-H) [76]. The binding of carbonate phases in the M3-CEC samples gave the material a slightly better binding compared to M3-AC and M3-HHC, even though they showed the highest porosity.

3.4. Effect of curing and carbonatization on the mineralogical and chemical composition

3.4.1. XRD and FTIR

A comparative analysis of XRD patterns of the M1 alkali-activated aggregates with the highest strengths is presented in Fig. 7a and revealed significant mineralogical changes during alkali activation and carbonatization. A prominent peak at 29.4° 2θ, corresponding to calcite ($CaCO_3$), was observed in all samples, primarily originating from unreactive crystalline calcite present in the BFA, but likely also formed as a carbonation product as indicated by variable intensities depending on the curing conditions. The lowest calcite intensity was detected in M1-AC, whereas the highest intensity appeared in M1-CEC, where accelerated carbonation for 28 days induced the most significant crystallization of stable calcite. It is worth noting that the intensity of the calcite peak increased slightly in M1-HCC compared to M1-AC, suggesting that under HCC conditions, characterized by higher temperature and humidity, mild carbonation occurred even at atmospheric CO_2 concentrations. Ca-rich alkali-activated systems under carbonatization predominantly form Ca-based carbonates [77]. The dissolution of CO_2 is enhanced in alkaline conditions, such as pore solution in an AAM system, leading to an increased concentration and availability of CO_3^{2-} [47,78].

The samples exposed to accelerated carbonation, M1-CEC and M1-PCC, exhibited a broad metacrystalline hump between 29.9° and 31.1° 2θ (Fig. 7a, marked with a dotted square), suggesting the formation of poorly crystalline or metastable carbonate-containing phases. The difference in carbonation exposure between M1-CEC (prolonged carbonation for 28 days) and M1-PCC (postponed carbonation for 14 days) indicates that extended CO_2 exposure promotes further ordering or even transformation of reactive phases into more structured carbonate forms. Furthermore, M1-CEC exhibits distinct additional peaks, suggesting a transition from metastable carbonate phases to aragonite, a less stable polymorph of $CaCO_3$, as indicated by additional reflections at 27.5° and 34.5° 2θ. The broad XRD region associated with metacrystalline carbonates suggests that not only pure Ca-carbonates but also other chemical elements, such as Mg and Na, are incorporated into carbonate phases of mixed chemical composition. The presence of altered carbonate phases at higher 2θ angles than calcite suggests lattice distortions [79,80], likely due to the inclusion of those impurities. This observation is consistent with the reactive composition of the precursor and activator, as shown in Table 1, Fig. 3, and Table S2.

The characteristic main peaks of lime (CaO, 32.2° 2θ) and anhydrite ($CaSO_4$, 33.5° 2θ), initially present in the BFA (Fig. 2a), were notably diminished in M1-AC, while in M1-HHC, M1-CEC, and M1-PCC, they were completely diminished likely due to accelerated reaction kinetics and higher degree reacted precursor.

Detailed FTIR spectra, presented in Fig. 7b, provided additional insights into the amorphous phase and further confirmed the

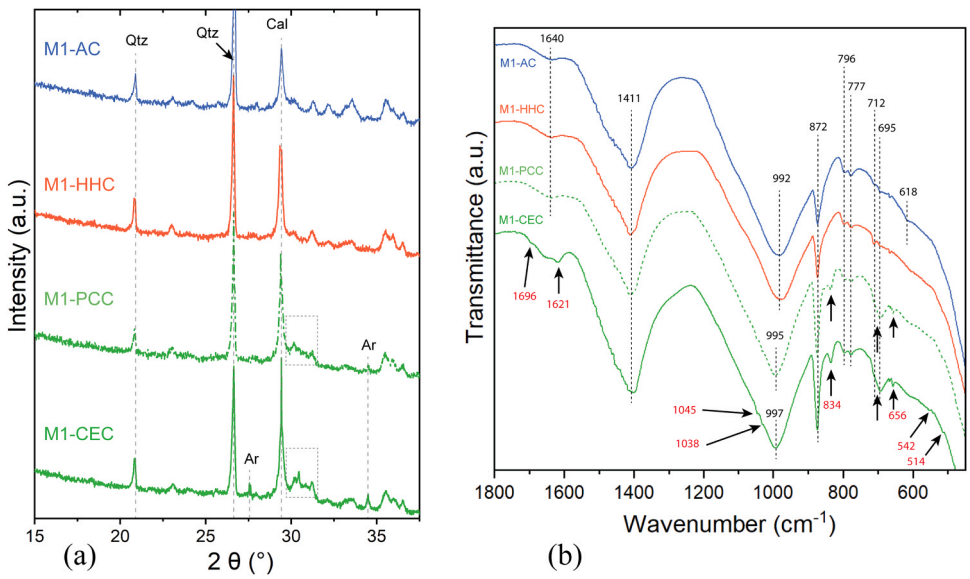

Fig. 7. (a) XRD patterns of AAM aggregates produced from M1, exhibiting the highest compressive strengths under different curing regimes. Qtz – quartz, Cal – calcite, Ar – aragonite. (b) FTIR spectra of the AAM aggregates produced from M1.

mineralogical data obtained from XRD (Fig. 7a). The main carbonate peaks observed at 1411 cm^{-1} correspond to asymmetric stretching, at 872 cm^{-1} to out-of-plane bending, and at 695 cm^{-1} and 712 cm^{-1} to in-plane bending vibrations of the C–O bond in carbonate ions (CO_3^{2-}) [81]. In M1-AC, these peaks primarily originate from pre-existing carbonate species. In contrast, M1-CEC and M1-PCC were exposed to elevated CO_2 concentrations, leading to more intense carbonate peaks due to increased $CaCO_3$ formation. Additionally, M1-CEC and M1-PCC have the appearance of a few new carbonate peaks: the 834 cm^{-1} peak, corresponding to out-of-plane bending, and the 656 cm^{-1} peak, associated with lattice vibrations of carbonate ions in less stable Ca-carbonate polymorphs like aragonite [82,83], as confirmed by XRD (Fig. 7a).

The main FTIR peak at approximately 990 cm^{-1} is a key feature in AAMs (Fig. 7b), associated with the stretching vibrations of Si–O–T bonds (T = Si or Al) in the aluminosilicate gel network. Upon alkali activation of the BFA and the formation of an aluminosilicate network, the main peak of the BFA precursor (Fig. S1 in the Supplementary Material, broader less intense peak at 1010 cm^{-1}) shifts towards lower wavenumbers with increased intensity (due to alkali-activation). Samples M1-AC and M1-HCC show a peak at around 990 cm^{-1}, while the carbonated samples 1CEC and 1PCC shift toward a higher wavenumber of 997 cm^{-1} and 995 cm^{-1}, respectively. Accelerated carbonation leads to the reaction of Ca^{2+} ions with CO_2 (dissolved in water as carbonate ion CO_3^{2-}), forming $CaCO_3$, according to Eq. (2), such as calcite, aragonite, or even vaterite in the initial phase.

$$Ca^{2+} + CO_2 + H_2O \rightarrow CaCO_3 + 2H^2 \quad (2)$$

In the M1-CEC sample, rapid carbonation significantly limited the formation of the alkali-activated matrix due to the extensive consumption of available Ca^{2+} for carbonate mineralization. This effect is also reflected in the reduced compressive strength compared to M1-HCC (Fig. 5a). As carbonation progressed, the remaining Ca^{2+} in the system became increasingly depleted, leading to the partial decalcification of the main AAM matrix phases, such as C-A-S-H gels. This process, driven by the preferential removal of Ca^{2+} from less stable hydrated gels, results in a shift of the Si–O–T peak to higher wavenumbers, known as a "blue shift" (Fig. 7b). As Ca is removed, weaker Ca–O bonds are replaced by stronger Si–O or Si–O–Al bonds, leading to a more ordered aluminosilicate network, similar to the behavior observed in low-Ca systems like metakaolin-based geopolymers [84]. In M1-CEC, where the Ca was preferentially used for CO_2 sequestration, two new minor FTIR peaks appear at higher wavenumbers, 1045 cm^{-1} and 1038 cm^{-1} , indicative of newly formed more Si-dominated phases as these peaks correspond to Si–O stretching vibrations. The presence of these low-intensity peaks, together with emerging very fine porosity, may indicate the formation of amorphous silica as a result of localized progressive Ca depletion within C-A-S-H gel itself (Eq. (3)) or possibly also as a result of insufficient Ca remaining for C-A-S-H gel formation after the precipitation of Ca carbonates. Small areas of almost pure Si-enriched phases observed in the M1-CEC sample with SEM-EDXS analysis are presented in Fig. S4 in the Supplementary Material, along with the corresponding cross-section explanation.

$$C\text{–}A\text{–}S\text{–}H + CO_2 \rightarrow (SiO_2 * Al_2O_3 * H_2O) + Ca^{2+} + OH^- \quad (3)$$

The band at 1640 cm^{-1}, observed in all aggregates, corresponds to the O–H bending vibration of water molecules, here in the form of a structurally bonded water within hydrate phases.

The M1-CEC sample produced two new peaks in the close O-H bending region, suggesting the formation of distinct hydrate phases. The bands at 1696 cm^{-1} and 1621 cm^{-1} correspond to C═O stretching, which is associated with carbonates, such as monohydrocalcite ($CaCO_3{\cdot}H_2O$, also referred to as hydrocalcite) [85,86] and/or nesquehonite ($MgCO_3{\cdot}3H_2O$) [87], where a layered carbonate structure contains interlayer water. Its main XRD peaks overlap with the primary calcite peak at 29.5° 2θ, making phase identification with XRD challenging. However, TG analysis can differentiate between carbonate phases.

M1-AC exhibits bending vibrations at 618 cm^{-1}, associated with sulfate ions (SO_4^{2-}) due to partially unreacted residual $CaSO_4$ (Fig. 7a, 33.5° 2θ), also observed in BFA FTIR spectra in Fig. S1 in Supplementary Material (617 cm^{-1}).

3.4.2. SEM-EDXS spatial chemical analysis of carbonation effects on the AAM matrix

The highly porous lightweight aggregates serve as an effective medium for CO_2 diffusion, enabling deeper penetration into the material and facilitating rapid interior carbonation. Dong et al. reported that dense, fly ash-based, 4 mm-sized AAM aggregates, with a

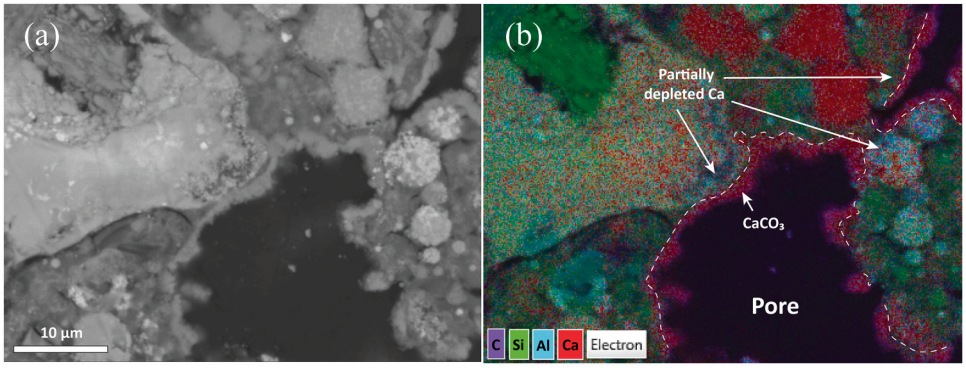

Fig. 8. (a) SEM micrograph of a cross-section and (b) EDXS mapping of the same area of M1-CEC sample, both at 2500 x magnification.

porosity below 3 %, required up to 30 days to achieve full carbonation [88]. In contrast, the highly porous structure of BFA aggregates significantly accelerates the carbonation process by enhancing CO_2 diffusion pathways. The crucial role of porosity in carbonation kinetics must be carefully considered, as faster carbonation is achieved due to the increased accessibility of reactive sites within the porous matrix. To achieve the desired properties, it is essential to adjust the time and conditions of accelerated carbonation accordingly. It is equally important to avoid overexposure, as exceeding the CO_2 sequestration potential can lead to wasted CO_2 during curing without additional benefits to the sustainability performance.

In carbonated AAM aggregates (M1-CEC and M1-PCC), a refinement of the pore diameter was observed, mainly due to $CaCO_3$ mineralization. The outer rim of the empty pore boundary is coated with a newly formed $CaCO_3$ layer (in Fig. 8b visible as a violet, interlayered distribution of Ca and C). The $CaCO_3$ encapsulation is 1–3 μm thick, which corresponds to a decrease in the large pore size diameter (Fig. 5a, M1-HCC vs. M1-CEC).

In the adjacent zone, where the old pore border interacted with pore fluid/gas, the Ca content is lower, indicating (partial) decalcification. The CO_2 diffusion through the interconnected pore network promoted localized carbonation, leading to the selective leaching of Ca^{2+} ions from this region. Ca-depleted areas appear less homogeneously structured in the SEM micrograph (Fig. 8a), suggesting fine-scale deterioration (also detected by MIP, Fig. 6a). This indicates that carbonation in this highly porous BFA-based AAM system leads to not only limited C-A-S-H gel formation but also decalciantion of remining Ca-risch AAM matrix, resulting in increased microporosity and structural changes.

In the M1-PCC sample, the first 14 days of HCC curing facilitated the formation of a resistant and dense C-A-S-H matrix, providing structural stability. During the subsequent 14 days of post-curing carbonation, the preferential formation of carbonates occurred without significant structural deterioration or notable alterations to the AAM matrix. As a result, partially carbonated AAM systems, such as the M1-PCC aggregates, were able to compensate for minor structural deterioration, exhibiting only a slight increase in total porosity and a lower degree of larger pore refinement (Fig. 6a,b). The minimal impact of post-curing carbonation suggests that the availability of Ca during the initial HCC phase enabled a robust C-A-S-H gel development, preventing major interaction with the matrix. Consequently, structural degradation remained barely detectable during the carbonation phase (Figs. 5d and 6a).

Multi-point EDXS analysis was conducted on the M1-HHC and M1-CEC samples to compare the non-carbonated and fully carbonated AAM aggregates with the highest mechanical strengths. The results, presented in Fig. 9 alongside the corresponding SEM micrographs, provide insights into the elemental distribution of the reacted matrix and changes induced by carbonation. In the M1-HHC sample, a large group of data points in the Si–Al–Ca ternary diagram falls within the range of 20–50 % Ca, 40–65 % Si, and ~10 % Al (Fig. 9b). The groped points are characteristic of main C-A-S-H gels, which form a dense alkali-activated matrix (Fig. 9a). C-A-S-H typically forms in alkali-activated systems with a Ca/Si ratio between 0.7 and 1.5 [89,90], suggesting a highly polymerized

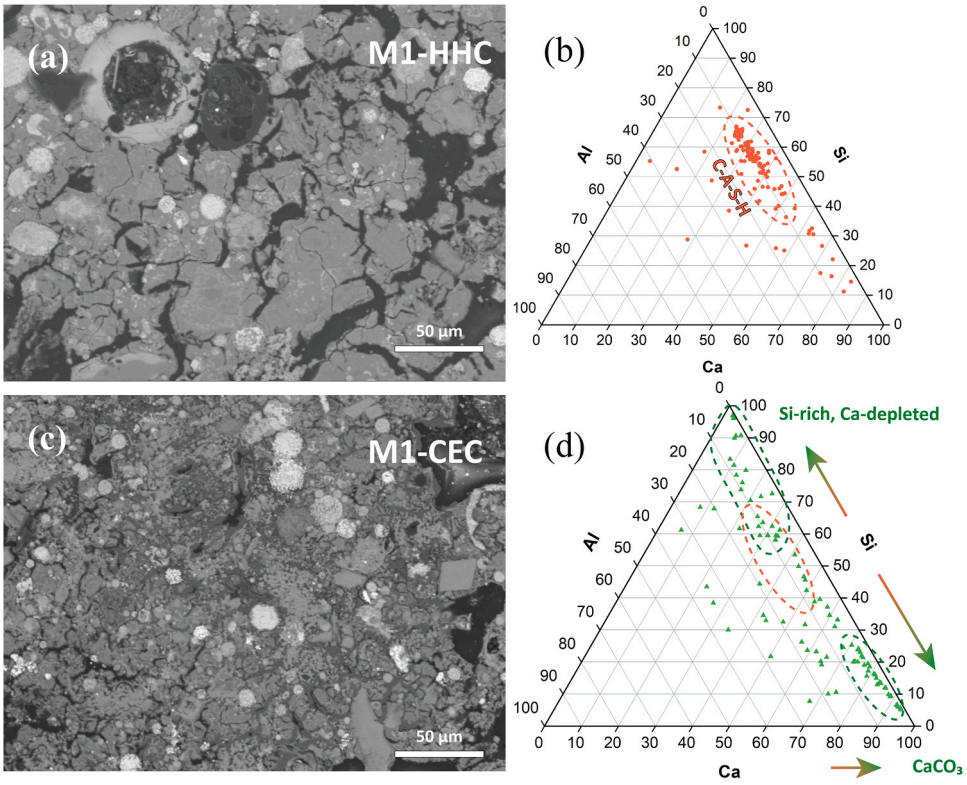

Fig. 9. SEM micrographs of AAM aggregates from M1 after 28 days of curing: (a) M1-HHC and (c) M1-CEC, along with their corresponding ternary diagrams (normalized Si:Al:Ca ratios) based on multi-point EDXS analysis of the matrix cross-section (b, d).

matrix, resulting in the highest compressive strength among all prepared AAM aggregates. The broad range of C-A-S-H gel compositions is likely due to differences in the local Si, Al, and Ca availability from the BFA precursor.

A significant composition shift is observed in the comparably analyzed M1-CEC sample, indicating extensive carbonation and limited C-A-S-H phase formation. The main C-A-S-H group observed in M1-HHC (Fig. 9b) is less pronounced in the case of M1-CEC, where a remaining scattered group of altered C-A-S-H with a low Ca/Si ratio also indicates partial Ca depletion. The Ca/Si ratio of the C-A-S-H phases after extensive carbonation is in the range of 0.38 – 0.75, where the limited availability of Ca during gel formation also restricts the agglomeration of C-A-S-H to fewer regions (fewer EDXS points were identified as C-A-S-H), as the available reactive system results in less interlayer Ca^{2+} ions, meaning weaker attractive forces [91]. A small group of points is observed with > 90 % Si, negligible Al and Ca indicate amorphous silica (also observed in Fig. S4, Supplementary Material), likely formed due to local almost complete decalcification. In contrast, a new dominant group, characterized by a high Ca/(Si+Al) ratio (above 2.7, up to 15.7), indicates the formation of $CaCO_3$ as a result of intensive carbonation. Consistent with the DTG peaks and XRD, those mainly correspond to calcite but also metastable carbonates (Fig. 7a).

The M1-CEC matrix cross-section (Fig. 9c) exhibits phase separation, where Ca-depleted phases appear darker compared to the more homogenous AAM matrix in M1-HHC (Fig. 9a). In backscattered electron detector with composition mode (BED-C), regions with lower atomic number elements (like Si and Al) appear darker, while Ca-rich phases (bright gray C-A-S-H, white $CaCO_3$) appear brighter [92]. However, it is important to note that the visual contrast in BED-C imaging is influenced not only by elemental composition but also by the average backscattering coefficient, which depends on the mean atomic number and, to some extent, also density. Thus, while variations in brightness can indicate differences in phase composition, they are only an indicator and not a definitive proof of elemental distribution, unlike the direct compositional data from systematic spatial EDXS analysis of the reacted matrix (Fig. 9b,d).

Partially carbonated AAM systems, such as M1-PCC aggregates, exhibit a minimal impact of post-curing carbonation, suggesting that the initial HCC curing phase enabled a C-A-S-H gel development, where after postponed carbonation degradation was not observed as final compressive strength was similar to M1-HCC (Fig. 5a,d).

3.4.3. *Thermogravimetric analysis*

The TG and derivative thermogravimetry (DTG, first derivate of the mass loss) curves of M1 AAM aggregates are presented in Fig. 10. In the 25–200°C range (I), the mass loss is primarily associated with the release of free and weakly bound water [93]. The M1-HCC sample exhibited the most pronounced peak in this region (Fig. 9b), likely indicating the presence of hydrates, which aligns with its compressive strength and XRD pattern of C-A-S-H formation (Figs. 4a and 6a). Similarly, the M1-PCC sample displayed a high peak, suggesting no significant changes in hydrated phases despite 14 days of post-carbonation. In contrast, the M1-CEC sample showed a significantly reduced peak, indicating a lower degree of C-A-S-H formation and/or lower free water content. The TG curve, in Fig. 10a, indicates that samples M1-HHC and M1-CEC exhibit higher mass loss before 400°C, which suggests the presence of C-(A)-S-H type reaction products [94].

In the M1-CEC sample, an additional significant peak appeared at approximately 130°C (II), which is attributed to interlayered water from monohydrocalcite and nesquehonite [87], indicating the presence of less stable hydrated carbonates. The formation of nesquehonite suggests that, in addition to Ca^{2+}, the presence of Mg^{2+} (as shown in Table 1 and Fig. 2, Mg from BFA) in an alkaline pH environment contributed to the carbonation process. Detecting these phases only in M1-CEC implies that the degree of Ca-depletion was high. Ca^{2+} is preferentially involved in carbonation, forming $CaCO_3$ polymorphs. However, as prolonged carbonation progresses, the Ca^{2+} availability decreases, and the system undergoes an equilibrium shift, allowing Mg^{2+} to participate in the formation of hydrated magnesium carbonates, such as nesquehonite ($MgCO_3 \cdot 3H_2O$).

The mass loss in the 400–625°C range (III) is associated with the breakdown of metastable carbonate phases (aragonite in M1-CEC and M1-PCC, Fig. 7a) and also the further decomposition of a (partially) altered AAM matrix [95,96].

The 625–800°C region (IV) corresponds to the decomposition of stable carbonates, primarily calcite. The M1-CEC sample exhibited the most pronounced peak, confirming prolonged carbonation, as also observed in the XRD patterns above. The M1-PCC sample

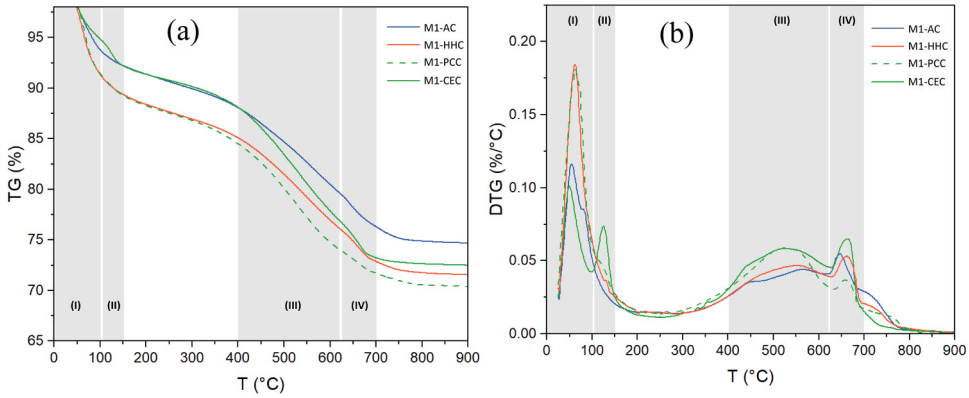

Fig. 10. (a) TG curves and (b) DTG curves of the M1 alkali-activated aggregates.

exhibited a weaker calcite peak, however, XRD and TG analysis confirmed the presence of metastable carbonates like aragonite and also some monohydrocalcite at lower temperatures. A minor peak in the 700–750°C range, observed in the M1-AC sample, is attributed to the decomposition of residual anhydrite or lime [97], as also supported by the FTIR spectra in Fig. 7b.

In contrast to the assessment of CO_2 sequestration in raw materials such as biomass wood ash [98], the broader and more complex mass loss observed with carbonated AAM aggregates within the 250–600°C range includes an overlapping decomposition of C-A-S-H, partially Ca-depleted phases, and metastable carbonates. Due to this complexity, quantifying the carbonation potential using the conventional thermal weight loss method in the 600–700°C range [99] was omitted, as it would not provide an accurate measure of CO_2 uptake.

3.4.4. Leaching of heavy metals

The raw BFA precursor exhibited low leaching concentrations of heavy metals (Table 5) such as As, Cr, Cu, Mn, Mo, Ni, and Pb, despite its highly alkaline pH of 12.65. However, the mobility of all measured heavy metals significantly increased upon alkali activation, except for Cu, which is known to remain relatively stable under highly alkaline conditions [100]. The high pH environment in AAMs can influence the mobilization of heavy metals, where oxyanion-forming elements (Cr, Mo) might particularly limit the use of waste in construction products. Mo and Cr have, e.g., exceeded regulatory limits set by national legislation on the permissible content of pollutants in the material in previous studies of industrial by-product valorization [101]. While regulations for the use of waste in construction differ or do not exist in some countries, the increased heavy metal leaching is a known issue with AAMs, particularly when using precursors with potentially hazardous trace elements [52,102]. The high pH of the alkali-activated environment leads to metal solubilization, increasing mobility and leaching potential.

The carbonation process in AAM aggregates produced from BFA played a crucial role in leaching mitigation through both physical and chemical immobilization mechanisms. The formation of $CaCO_3$ encapsulation around pores (Fig. 8) effectively reduced the exposed reactive surface area, even though the aggregates were crushed for the leaching tests. In real-world applications, these aggregates would be used in their intact form, i.e., leaching should be even lower, as the intact carbonate layer would limit exposure. Physical immobilization restricts the contact between the material and the leaching solution, thereby reducing metal release. Additionally, the formation of calcium carbonates lowered the pH of the AAMs, as shown in Table 5, promoting chemical immobilization by reducing the solubility of certain heavy metals, particularly Cr.

This effect is evident when comparing M1-CEC to M1-HCC, where only the CO_2 exposure influences the differences in leaching behavior. Among the tested samples, M1-CEC (carbonated for 28 d) exhibited the lowest heavy metal leaching, confirming the efficiency of carbonation as a stabilization mechanism. The M1-PCC sample, post-carbonated for 14 d, showed a similar leaching mitigation effect, demonstrating that even partial carbonation is effective in immobilizing heavy metals.

Besides the evident leaching mitigation mechanism by pH reduction and physical encapsulation, other effects of mineral carbonation could also be considered, such as the immobilisation of heavy metals by co-precipitation in carbonates [103]. In addition, some studies suggest that carbonation products such as silica gel can be considered as adsorbents for metals [104,105], where in the case of the M1-CEC sample some phases with $>$ 90 % Si and negligible Al and Ca were formed (Fig. 9d, Fig. S4, Supplementary Material).

4. Conclusions

Lightweight alkali-activated aggregates with densities ranging below 1.6 g/cm^3 and compressive strengths up to 1.1 MPa were produced from biomass fly ash (BFA) without secondary precursors. The pelletization process crucially affected the aggregate porosity; a two-step rotational speed approach achieved the higher pelletization efficiency while maintaining a porosity between 45–59 %. The initial low-speed phase facilitated nucleation, while the subsequently increased rotational speed prevented excessive compaction while preserving an open and porous structure. The highly porous nature of the aggregates provided a suitable medium for CO_2 diffusion, enabling rapid carbonation via interconnected pores.

The alkali activator content significantly influenced both the strength development and pelletization efficiency. Aggregates with an activator (M1, M2) exhibited higher strengths than those without it (M3), confirming that a Si:Al ratio of 1.9 promoted the formation of a well-developed C-A-S-H binding matrix. Despite a fixed w/s ratio, the alkali content in the activator solution enhanced the pelletization efficiency by improving the liquid bridge formation and initiating early-stage reactions.

The interaction between carbonation and alkali activation was crucial for achieving the mechanical properties and microstructure. Carbonation refined the pore structure through $CaCO_3$ mineralization but also impacted the C-A-S-H formation. Aggregates carbonated immediately after production (M1-CEC) experienced a Ca^{2+} depletion due to rapid carbonate formation, limiting the C-A-S-H development and reducing the compressive strength. With a prolonged carbonation for 28 days, the structural degradation became evident due to a partial C-A-S-H decalcification and an increased microporosity. The presence of Mg carbonates suggested a Mg incorporation in response to Ca depletion. In contrast, M1-PCC aggregates carbonated after 14 days exhibited a more stable structure, as the initial high-temperature curing (HHC) process allowed the C-A-S-H gel to develop before carbonation, mitigating adverse effects.

Despite the strength reduction observed in prolonged CO_2-cured aggregates, M1-CEC still outperformed ambient-cured (AC) aggregates, which exhibited the lowest compressive strength. Notably, the aggregates cured under heat and humidity (M1-HHC) and those subjected to postponed carbonation after 14 days of heat and humidity curing (M1-PCC) achieved compressive strengths exceeding 1 MPa, demonstrating a viable method for producing lightweight aggregates solely from BFA, without the need for secondary precursors.

Microstructural analysis confirmed that carbonation promotes mineralization, forming an encapsulating layer that refines larger

Table 5
Leaching measurements of the M1 aggregates, showing the concentrations of leached heavy metals and pH values of the water suspension.

Sample	As [mg/l]	Cr [mg/l]	Cu [mg/l]	Mn [mg/l]	Mo [mg/l]	Ni [mg/l]	Pb [mg/l]	pH
BFA	0.005	0.003	0.006	0.002	0.008	0.003	0.028	12.65
M1-AC	1.078	0.062	0.007	0.011	0.164	0.004	0.029	12.32
M1-HHC	1.115	0.228	0.007	0.017	0.197	0.006	0.049	12.36
M1-CEC	**0.550**	**0.004**	0.007	**0.008**	**0.162**	**0.002**	**0.031**	10.22
M1-PCC	**0.258**	**0.004**	0.007	**0.006**	**0.178**	**0.003**	**0.030**	10.25

pores. However, fully carbonated M1-CEC exhibited increased microporosity due to a reduced C-A-S-H matrix with phase separation and local decalcification. Multi-point EDXS analysis confirmed compositional shifts in fully carbonated samples, where, besides lower Ca/Si C-A-S-H, $CaCO_3$ carbonates and Ca-depleted phases emerged due to prolonged accelerated carbonation. TG analysis further revealed that prolonged carbonated M1-CEC contained hydrated carbonate phases, including nesquehonite, suggesting Mg^{2+} incorporation as a result of Ca depletion.

Carbonation significantly reduced heavy metal leaching, primarily through $CaCO_3$ encapsulation and pH reduction. The M1-PCC sample demonstrated that even postponed carbonation after 14 days provided similar leaching mitigation as the fully carbonated sample M1-CEC, emphasizing that controlled carbonation can enhance the environmental performance while preserving the compressive strength.

Overall, the high porosity and interconnected pore structure make alkali-activated BFA aggregates particularly effective for CO_2 sequestration and lightweight applications. In addition to non-structural construction elements (e.g., lightweight concrete, panels, insulation layers), they also show potential for applications in horticulture, filtration media, and acoustic insulation. Additionally, the combination of alkali activation and carbonation offers a potential strategy for stable lightweight materials and reducing environmental impacts, where the complex interplay between alkali activation and carbonation requires optimization to maintain optimal mechanical performance, CO_2 storage potential, and leaching mitigation.

CRediT authorship contribution statement

Vilma Ducman: Writing – review & editing, Writing – original draft, Validation, Supervision, Resources, Conceptualization. **Lisbeth M. Ottosen:** Writing – review & editing, Methodology, Data curation. **Anže Tesovnik:** Writing – review & editing, Writing – original draft, Visualization, Validation, Methodology, Investigation, Formal analysis, Data curation, Conceptualization.

Declaration of Competing Interest

The authors declare that they have no known competing financial interests or personal relationships that could have appeared to influence the work reported in this paper.

Acknowledgements

This research was EU-funded by the ASHCYCLE project, under grant number 101058162. Anže Tesovnik is supported by the Young Researcher Program within the ARIS Program Group P2-0273. Laboratory technician Ebba Cederberg Schnell from the Department of Civil Engineering, Technical University of Denmark is thanked for analytical help with leaching experiments. The authors would also like to thank Dr. Sara Tominc from the Slovenian National Building and Civil Engineering Institute for performing the TG measurements.

Appendix A. Supporting information

Supplementary data associated with this article can be found in the online version at doi:10.1016/j.cscm.2025.e05014.

Data availability

The complete raw measurement dataset for this study is openly accessible in the DiRROS repository at the following link: http://hdl.handle.net/20.500.12556/DiRROS-22660.

References

[1] P.J.M. Monteiro, S.A. Miller, A. Horvath, Towards sustainable concrete, Nat. Mater. 16 (2017) 698–699, https://doi.org/10.1038/nmat4930.
[2] K.T. Adams, M. Osmani, T. Thorpe, J. Thornback, Circular economy in construction: current awareness, challenges and enablers, Proc. Inst. Civ. Eng. Waste Resour. Manag. 170 (2017) 15–24, https://doi.org/10.1680/jwarm.16.00011.

[3] Directive 2009/28/EC of the European Parliament and of the Council of 23 April 2009 on the promotion of the use of energy from renewable sources and amending and subsequently repealing Directives 2001/77/EC and 2003/30/EC (Text with EEA relevance), 2009. ⟨http://data.europa.eu/eli/dir/2009/28/oj/eng⟩ (Accessed 28 November 2024).
[4] L.J.R. Nunes, J.C.O. Matias, J.P.S. Catalão, Biomass in the generation of electricity in Portugal: a review, Renew. Sustain. Energy Rev. 71 (2017) 373–378, https://doi.org/10.1016/j.rser.2016.12.067.
[5] K. Trivedi, A. Sharma, B.K. Kanabar, K.D. Arunachalam, S. Gautam, Comparative analysis of coal and biomass for sustainable energy production: elemental composition, combustion behavior and co-firing potential, Water Air Soil Pollut. 235 (2024) 698, https://doi.org/10.1007/s11270-024-07509-3.
[6] F. Si, H. Zhang, X. Feng, Y. Xu, L. Zhang, L. Zhao, L. Li, Thermodynamics and synergistic effects on the co-combustion of coal and biomass blends, J. Therm. Anal. Calor. 149 (2024) 7749–7761, https://doi.org/10.1007/s10973-024-13310-5.
[7] S. Knapp, A. Güldemund, S. Weyand, L. Schebek, Evaluation of co-firing as a cost-effective short-term sustainable CO2 mitigation strategy in Germany, Energy Sustain. Soc. 9 (2019) 32, https://doi.org/10.1186/s13705-019-0214-3.
[8] J. Zhai, I.T. Burke, D.I. Stewart, Beneficial management of biomass combustion ashes, Renew. Sustain. Energy Rev. 151 (2021) 111555, https://doi.org/10.1016/j.rser.2021.111555.
[9] ⟨https://www.worldbioenergy.org/uploads/241023%20GBS%20Report%20Short%20Version.pdf⟩, (n.d.). ⟨https://www.worldbioenergy.org/uploads/241023%20GBS%20Report%20Short%20Version.pdf⟩ (Accessed 28 November 2024).
[10] J. Wierzbowska, S. Sienkiewicz, P. Żarczyński, S. Krzebietke, Environmental application of ash from incinerated biomass, Agronomy 10 (2020) 482, https://doi.org/10.3390/agronomy10040482.
[11] F.R. Kurzemann, M.F.-D. Juárez, M. Probst, M. Gómez-Brandón, H. Spiegel, R. Resch, H. Insam, E.M. Pötsch, Biomass ash as a substitute for lime and its impact on grassland soil, forage, and soil microbiota, Agronomy 14 (2024) 1568, https://doi.org/10.3390/agronomy14071568.
[12] Best Management Practices for Wood Ash as Agricultural Soil Amendment, (n.d.). ⟨https://extension.uga.edu/publications/detail.html?number=B1142&title=best-management-practices-for-wood-ash-as-agricultural-soil-amendment⟩ (Accessed 28 November 2024).
[13] D. Nagrockienė, A. Daugėla, Investigation into the properties of concrete modified with biomass combustion fly ash, Constr. Build. Mater. 174 (2018) 369–375, https://doi.org/10.1016/j.conbuildmat.2018.04.125.
[14] V. Sklivaniti, P.E. Tsakiridis, N.S. Katsiotis, D. Velissariou, N. Pistofidis, D. Papageorgiou, M. Beazi, Valorisation of woody biomass bottom ash in Portland cement: a characterization and hydration study, J. Environ. Chem. Eng. 5 (2017) 205–213, https://doi.org/10.1016/j.jece.2016.11.042.
[15] E.R. Teixeira, A. Camões, F.G. Branco, Valorisation of wood fly ash on concrete, Resour. Conserv. Recycl. 145 (2019) 292–310, https://doi.org/10.1016/j.resconrec.2019.02.028.
[16] R. Rajamma, R.J. Ball, L.A.C. Tarelho, G.C. Allen, J.A. Labrincha, V.M. Ferreira, Characterisation and use of biomass fly ash in cement-based materials, J. Hazard. Mater. 172 (2009) 1049–1060, https://doi.org/10.1016/j.jhazmat.2009.07.109.
[17] C.B. Cheah, M. Ramli, The implementation of wood waste ash as a partial cement replacement material in the production of structural grade concrete and mortar: an overview, Resour. Conserv. Recycl. 55 (2011) 669–685, https://doi.org/10.1016/j.resconrec.2011.02.002.
[18] M. Berra, T. Mangialardi, A.E. Paolini, Reuse of woody biomass fly ash in cement-based materials, Constr. Build. Mater. 76 (2015) 286–296, https://doi.org/10.1016/j.conbuildmat.2014.11.052.
[19] J.L. Provis, Alkali-activated materials, Cem. Concr. Res. 114 (2018) 40–48, https://doi.org/10.1016/j.cemconres.2017.02.009.
[20] P. Duxson, J.L. Provis, G.C. Lukey, S.W. Mallicoat, W.M. Kriven, J.S.J. van Deventer, Understanding the relationship between geopolymer composition, microstructure and mechanical properties, Colloids Surf. A Physicochem. Eng. Asp. 269 (2005) 47–58, https://doi.org/10.1016/j.colsurfa.2005.06.060.
[21] V. Viola, A. D'Angelo, L. Vertuccio, M. Catauro, Metakaolin-based geopolymers filled with industrial wastes: improvement of physicochemical properties through sustainable waste recycling, Polymers 16 (2024) 2118, https://doi.org/10.3390/polym16152118.
[22] T. Luukkonen, Y. Yu, S.K. Adhikary, S. Kauppinen, M. Finnilä, P. Perumal, Metallic aluminium in municipal solid waste incineration fly ash as a blowing agent for porous alkali-activated granules, R. Soc. Open Sci. 11 (2024) 240598, https://doi.org/10.1098/rsos.240598.
[23] S. Zhang, A. Keulen, K. Arbi, G. Ye, Waste glass as partial mineral precursor in alkali-activated slag/fly ash system, Cem. Concr. Res. 102 (2017) 29–40, https://doi.org/10.1016/j.cemconres.2017.08.012.
[24] M. Mastali, A. Zahra, K. Hugo, R. Faraz, Utilization of mineral wools in production of alkali activated materials, Constr. Build. Mater. 283 (2021) 122790, https://doi.org/10.1016/j.conbuildmat.2021.122790.
[25] A. Fernández-Jiménez, N. Cristelo, T. Miranda, Á. Palomo, Sustainable alkali activated materials: Precursor and activator derived from industrial wastes, J. Clean. Prod. 162 (2017) 1200–1209, https://doi.org/10.1016/j.jclepro.2017.06.151.
[26] Filling Fresh Metakaolin-Based Geopolymer Paste with Wood Ash: Chemical and Mechanical Characterization - Catauro - 2024 - Macromolecular Symposia - Wiley Online Library, (n.d.). ⟨https://onlinelibrary.wiley.com/doi/10.1002/masy.202300252⟩ (Accessed 2 December 2024).
[27] S. Kumar Das, A. Adediran, C. Rodrigue Kaze, S. Mohammed Mustakim, N. Leklou, Production, characteristics, and utilization of rice husk ash in alkali activated materials: an overview of fresh and hardened state properties, Constr. Build. Mater. 345 (2022) 128341, https://doi.org/10.1016/j.conbuildmat.2022.128341.
[28] Z. Liu, P. Deng, Z. Zhang, Application of silica-rich biomass ash solid waste in geopolymer preparation: a review, Constr. Build. Mater. 356 (2022) 129142, https://doi.org/10.1016/j.conbuildmat.2022.129142.
[29] V. Athira, V. Charitha, G. Athira, A. Bahurudeen, Agro-waste ash based alkali-activated binder: cleaner production of zero cement concrete for construction, J. Clean. Prod. 286 (2021) 125429, https://doi.org/10.1016/j.jclepro.2020.125429.
[30] K.G. Santhosh, S.M. Subhani, A. Bahurudeen, Sustainable reuse of palm oil fuel ash in concrete, alkali-activated binders, soil stabilisation, bricks and adsorbent: A waste to wealth approach, Ind. Crops Prod. 183 (2022) 114954, https://doi.org/10.1016/j.indcrop.2022.114954.
[31] L. Soriano, A. Font, M.V. Borrachero, J.M. Monzó, J. Payá, M.M. Tashima, Biomass ashes to produce an alternative alkaline activator for alkali-activated cements, Mater. Lett. 308 (2022) 131198, https://doi.org/10.1016/j.matlet.2021.131198.
[32] K. Tamanna, S.N. Raman, M. Jamil, R. Hamid, Utilization of wood waste ash in construction technology: a review, Constr. Build. Mater. 237 (2020) 117654, https://doi.org/10.1016/j.conbuildmat.2019.117654.
[33] M. Catauro, V. Viola, A. D'Amore, Filling fresh metakaolin-based geopolymer paste with wood ash: chemical and mechanical characterization, Macromol. Symp. 413 (2024) 2300252, https://doi.org/10.1002/masy.202300252.
[34] D. Eliche-Quesada, A. Calero-Rodríguez, E. Bonet-Martínez, L. Pérez-Villarejo, P.J. Sánchez-Soto, Geopolymers made from metakaolin sources, partially replaced by Spanish clays and biomass bottom ash, J. Build. Eng. 40 (2021) 102761, https://doi.org/10.1016/j.jobe.2021.102761.
[35] A. Natali Murri, V. Medri, E. Papa, L. Laghi, C. Mingazzini, E. Landi, Porous geopolymer insulating core from a metakaolin/biomass ash composite, Environments 4 (2017) 86, https://doi.org/10.3390/environments4040086.
[36] J. Pokorný, L. Zemanová, M. Pavlíková, Z. Pavlík, Properties of alkali-activated composites containing biomass ash, AIP Conf. Proc. 2170 (2019) 020016, https://doi.org/10.1063/1.5132735.
[37] L.-P. Qian, L.-Y. Xu, B.-T. Huang, Y. Li, J. Lan, F. Gong, H. Guan, Functionalization of waste-derived artificial aggregates: a state-of-the-art review, Resour. Conserv. Recycl. 212 (2025) 107999, https://doi.org/10.1016/j.resconrec.2024.107999.
[38] G.B. Bekkeri, K.K. Shetty, G. Nayak, Synthesis of artificial aggregates and their impact on performance of concrete: a review, J. Mater. Cycles Waste Manag 25 (2023) 1988–2011, https://doi.org/10.1007/s10163-023-01713-9.
[39] L.-P. Qian, L.-Y. Xu, B.-T. Huang, J.-G. Dai, Pelletization and properties of artificial lightweight geopolymer aggregates (GPA): One-part *vs.* two-part geopolymer techniques, J. Clean. Prod. 374 (2022) 133933, https://doi.org/10.1016/j.jclepro.2022.133933.
[40] L.-P. Qian, L.-Y. Xu, Y. Alrefaei, T. Wang, T. Ishida, J.-G. Dai, Artificial alkali-activated aggregates developed from wastes and by-products: a state-of-the-art review, Resour. Conserv. Recycl. 177 (2022) 105971, https://doi.org/10.1016/j.resconrec.2021.105971.
[41] O. Rudić, V. Ducman, M. Malešev, V. Radonjanin, S. Draganić, S. Šupić, M. Radeka, Aggregates obtained by alkali activation of fly ash: the effect of granulation, pelletization methods and curing regimes, Materials 12 (2019) 776, https://doi.org/10.3390/ma12050776.

[42] G.B. Bekkeri, K.K. Shetty, G. Nayak, Producing of alkali-activated artificial aggregates by pelletization of fly ash, slag, and seashell powder, Innov. Infrastruct. Solut. 8 (2023) 258, https://doi.org/10.1007/s41062-023-01227-1.

[43] Biswaroop Ghosh, Dr.A.K. Rath, KIIT university, fly-ash pellets as a replacement of coarse aggregate in concrete mixture, IJERT V6 (2017), https://doi.org/10.17577/IJERTV6IS080155. IJERTV6IS080155.

[44] V. Ducman a, M. Radeka, Alkali activated green building materials – selected case study of alkali activated aggregate, Ceram. Mod. Technol. 1 (2019), https://doi.org/10.29272/cmt.2018.0006.

[45] M. Gesoğlu, E. Güneyisi, H.Ö. Öz, Properties of lightweight aggregates produced with cold-bonding pelletization of fly ash and ground granulated blast furnace slag, Mater. Struct. 45 (2012) 1535–1546, https://doi.org/10.1617/s11527-012-9855-9.

[46] M. Tonelli, R. Camerini, P. Baglioni, F. Ridi, Activation of ground granulated blast-furnace slag with calcium hydroxide nanoparticles towards the consolidation of adobe, Constr. Build. Mater. 439 (2024) 137285, https://doi.org/10.1016/j.conbuildmat.2024.137285.

[47] P. Nielsen, M. Quaghebeur, Determination of the CO2 uptake of construction products manufactured by mineral carbonation, Minerals 13 (2023) 1079, https://doi.org/10.3390/min13081079.

[48] J. Davidovits, Geopolymers: ceramic-like inorganic polymers, J. Ceram. Sci. Technol. 8 (2017) 335–350, https://doi.org/10.4416/JCST2017-00038.

[49] P. Azarsa, R. Gupta, Durability and leach-ability evaluation of K-based geopolymer concrete in real environmental conditions, Case Stud. Constr. Mater. 13 (2020) e00366, https://doi.org/10.1016/j.cscm.2020.e00366.

[50] B. Li, S. Jian, J. Zhu, X. Gao, W. Gao, Effect of sintering temperature on lightweight aggregates manufacturing from copper contaminated soil, Ceram. Int. 47 (2021) 31319–31328, https://doi.org/10.1016/j.ceramint.2021.08.005.

[51] C.R. Cheeseman, C.J. Sollars, S. McEntee, Properties, microstructure and leaching of sintered sewage sludge ash, Resour. Conserv. Recycl. 40 (2003) 13–25, https://doi.org/10.1016/S0921-3449(03)00022-3.

[52] I. Lancellotti, E. Kamseu, M. Michelazzi, L. Barbieri, A. Corradi, C. Leonelli, Chemical stability of geopolymers containing municipal solid waste incinerator fly ash, Waste Manag. 30 (2010) 673–679, https://doi.org/10.1016/J.WASMAN.2009.09.032.

[53] L.M. Ottosen, N.M. Sigvardsen, Heavy metal leaching from wood ash before and after hydration and carbonation, Environ. Sci. Pollut. Res (2024), https://doi.org/10.1007/s11356-024-33221-0.

[54] S. Geetha, K. Ramamurthy, Properties of geopolymerised low-calcium bottom ash aggregate cured at ambient temperature, Cem. Concr. Compos. 43 (2013) 20–30, https://doi.org/10.1016/j.cemconcomp.2013.06.007.

[55] K.N. Shivaprasad, B.B. Das, Determination of optimized geopolymerization factors on the properties of pelletized fly ash aggregates, Constr. Build. Mater. 163 (2018) 428–437, https://doi.org/10.1016/j.conbuildmat.2017.12.038.

[56] B. Horvat, V. Ducman, Potential of green ceramics waste for alkali activated foams, Materials 12 (2019) 3563, https://doi.org/10.3390/ma12213563.

[57] L. Dembovska, D. Bajare, V. Ducman, L. Korat, G. Bumanis, The use of different by-products in the production of lightweight alkali activated building materials, Constr. Build. Mater. 135 (2017) 315–322, https://doi.org/10.1016/j.conbuildmat.2017.01.005.

[58] A.S. Srinivasa, K. Swaminathan, S.C. Yaragal, Effect of water to geopolymer solids ratio on properties of fly ash and slag-based one-part geopolymer binders, Res. Transcr. Mater. 2 (2024) 81–92, https://doi.org/10.55084/grinrey/RTM/978-81-964105-5-1_6.

[59] M. Mohammed, A.J.M. Jawad, A.M. Mohammed, J.K. Oleiwi, T. Adam, A.F. Osman, O.S. Dahham, B.O. Betar, S.C.B. Gopinath, M. Jaafar, Challenges and advancement in water absorption of natural fiber-reinforced polymer composites, Polym. Test. 124 (2023) 108083, https://doi.org/10.1016/j.polymertesting.2023.108083.

[60] A. Ferraro, F. Colangelo, I. Farina, M. Race, R. Cioffi, C. Cheeseman, M. Fabbricino, Cold-bonding process for treatment and reuse of waste materials: technical designs and applications of pelletized products, Crit. Rev. Environ. Sci. Technol. 51 (2021) 2197–2231, https://doi.org/10.1080/10643389.2020.1776052.

[61] N.U. Kockal, T. Ozturan, Effects of lightweight fly ash aggregate properties on the behavior of lightweight concretes, J. Hazard. Mater. 179 (2010) 954–965, https://doi.org/10.1016/j.jhazmat.2010.03.098.

[62] EN 1097-3:1998 - Tests for mechanical and physical properties of aggregates - Part 3: Determination of loose bulk density and voids, iTeh Standards (n.d.). ⟨https://standards.iteh.ai/catalog/standards/cen/1e043df4-6c8e-423c-9ba7-3bcb715a6cf3/en-1097-3-1998⟩ (accessed 10 January 2025).

[63] SIST EN 12457-4:2004 - Characterisation of waste - Leaching - Compliance test for leaching of granular waste materials and sludges - Part 4: One stage batch test at a liquid to solid ratio of 10 l/kg for materials with particle size below 10 mm (without or with size reduction), iTeh Standards (n.d.). ⟨https://standards.iteh.ai/catalog/standards/sist/545ddfc4-33b5-4710-a3f3-f17cbbf51c00/sist-en-12457-4-2004⟩ (Accessed 16 January 2025).

[64] A. Ferraro, V. Ducman, F. Colangelo, L. Korat, D. Spasiano, I. Farina, Production and characterization of lightweight aggregates from municipal solid waste incineration fly-ash through single- and double-step pelletization process, J. Clean. Prod. 383 (2023) 135275, https://doi.org/10.1016/j.jclepro.2022.135275.

[65] S. Ebnesajjad, 3 - surface tension and its measurement, in: S. Ebnesajjad (Ed.), Handbook of Adhesives and Surface Preparation, William Andrew Publishing, Oxford, 2011, pp. 21–30, https://doi.org/10.1016/B978-1-4377-4461-3.10003-3.

[66] T. Luukkonen, Z. Abdollahnejad, J. Yliniemi, P. Kinnunen, M. Illikainen, One-part alkali-activated materials: a review, Cem. Concr. Res. 103 (2018) 21–34, https://doi.org/10.1016/j.cemconres.2017.10.001.

[67] P. Duxson, S.W. Mallicoat, G.C. Lukey, W.M. Kriven, J.S.J. van Deventer, The effect of alkali and Si/Al ratio on the development of mechanical properties of metakaolin-based geopolymers, Colloids Surf. A Physicochem. Eng. Asp. 292 (2007) 8–20, https://doi.org/10.1016/j.colsurfa.2006.05.044.

[68] H. Wang, H. Wu, Z. Xing, R. Wang, S. Dai, The effect of various Si/Al, Na/Al molar ratios and free water on micromorphology and macro-strength of metakaolin-based geopolymer, Materials 14 (2021) 3845, https://doi.org/10.3390/ma14143845.

[69] M. Češnovar, K. Traven, B. Horvat, V. Ducman, The potential of ladle slag and electric arc furnace slag use in synthesizing alkali activated materials; the influence of curing on mechanical properties, Materials 12 (2019) 1173, https://doi.org/10.3390/ma12071173.

[70] Leca® Lightweight Aggregate Concrete - LWAC, (n.d.). ⟨https://www.leca.co.uk/products/Leca%C2%AE-Lightweight-Aggregate-Concrete⟩ (Accessed 11 June 2025).

[71] A. Zukri, R. Nazir, K.N.M. Said, H. Moayedi, Physical and Mechanical Properties of Lightweight Expanded Clay Aggregate (LECA), MATEC Web Conf. 250 (2018) 01016, https://doi.org/10.1051/matecconf/201825001016.

[72] 2023 Florida Building Code, Building, Eighth Edition - CHAPTER 19 CONCRETE - SECTION 1917 LIGHTWEIGHT INSULATING CONCRETE ROOFS, (n.d.). ⟨https://codes.iccsafe.org/s/FLBC2023P1/chapter-19-concrete/FLBC2023P1-Ch19-Sec1917⟩ (Accessed 11 June 2025).

[73] A. Frankovič, V. Bokan Bosiljkov, V. Ducman, Lightweight aggregates made from fly ash using the cold-bond process and their use in lightweight concrete, Mater. Teh. 51 (2017) 267–274, https://doi.org/10.17222/mit.2015.337.

[74] A. Masłoń, M. Cieśla, R. Gruca-Rokosz, L. Bichajło, A. Nowotnik, M. Pytel, K. Gancarczyk, M. Chutkowski, M. Potoczek, M. Franus, K. Kalinowska-Wichrowska, Lightweight artificial aggregates produced from water reservoir sediment and industrial waste—ecological and technological aspect, Materials 18 (2025) 2563, https://doi.org/10.3390/ma18112563.

[75] P. Risdanareni, J. Wang, N. Boon, N. De Belie, Alkali activated lightweight aggregate as bacterial carrier in manufacturing self-healing mortar, Constr. Build. Mater. 368 (2023) 130375, https://doi.org/10.1016/j.conbuildmat.2023.130375.

[76] H.G. Tural, B. Ozarisoy, S. Derogar, C. Ince, Investigating the governing factors influencing the pozzolanic activity through a database approach for the development of sustainable cementitious materials, Constr. Build. Mater. 411 (2024) 134253, https://doi.org/10.1016/j.conbuildmat.2023.134253.

[77] S. Shagñay, A. Bautista, F. Velasco, M. Torres-Carrasco, Carbonation of alkali-activated and hybrid mortars manufactured from slag: Confocal Raman microscopy study and impact on wear performance, BoletíN. De. La Soc. Española De. Cerámica Y. Vidr. 62 (2023) 428–442, https://doi.org/10.1016/j.bsecv.2022.07.003.

[78] S.H. Han, Y. Jun, J.H. Kim, The use of alkaline CO2 solvent for the CO2 curing of blast-furnace slag mortar, Constr. Build. Mater. 342 (2022) 127977, https://doi.org/10.1016/j.conbuildmat.2022.127977.

[79] R.B.C. Dardo, R.J. Jagus, M. Imura, R.G. Banal, X-ray diffraction line profile analysis of natural calcite minerals found in Southern Philippines by Williamson-Hall Method, J. Eng. Environ. Agric. Res. 3 (2024) 29–37, https://doi.org/10.34002/jeear.v3i1.82.

[80] B. Pokroy, A.N. Fitch, P.L. Lee, J.P. Quintana, E.N. Caspi, E. Zolotoyabko, Anisotropic lattice distortions in the mollusk-made aragonite: a widespread phenomenon, J. Struct. Biol. 153 (2006) 145–150, https://doi.org/10.1016/j.jsb.2005.10.009.
[81] L. Fernández-Carrasco, D. Torrens-Martín, L.M. Morales, S. Martínez-Ramírez, L. Fernández-Carrasco, D. Torrens-Martín, L.M. Morales, S. Martínez-Ramírez, Infrared spectroscopy in the analysis of building and construction materials, in: Infrared Spectroscopy - Materials Science, Engineering and Technology, IntechOpen, 2012 https://doi.org/10.5772/36186.
[82] M.B. Toffolo, L. Regev, S. Dubernet, Y. Lefrais, E. Boaretto, FTIR-based crystallinity assessment of aragonite–calcite mixtures in archaeological lime binders altered by diagenesis, Minerals 9 (2019) 121, https://doi.org/10.3390/min9020121.
[83] D. Chakrabarty, S. Mahapatra, Aragonite crystals with unconventional morphologies, J. Mater. Chem. J. Mater. Chem. 9 (1999) 2953–2957, https://doi.org/10.1039/a905407c.
[84] I. Ozer, S. Soyer-Uzun, Relations between the structural characteristics and compressive strength in metakaolin based geopolymers with different molar Si/Al ratios, Ceram. Int. 41 (2015) 10192–10198, https://doi.org/10.1016/j.ceramint.2015.04.125.
[85] J. Pan, H. Zhao, M.E. Tucker, J. Zhou, M. Jiang, Y. Wang, Y. Zhao, B. Sun, Z. Han, H. Yan, Biomineralization of monohydrocalcite induced by the halophile halomonas smyrnensis WMS-3, Minerals 9 (2019) 632, https://doi.org/10.3390/min9100632.
[86] R. Chaliulina, Precipitated Calcium Carbonate: Recycling Carbon Dioxide and Industrial Waste Brines, 2019. https://doi.org/10.13140/RG.2.2.27644.05765.
[87] H. Ren, Z. Chen, Y. Wu, M. Yang, J. Chen, H. Hu, J. Liu, Thermal characterization and kinetic analysis of nesquehonite, hydromagnesite, and brucite, using TG–DTG and DSC techniques, J. Therm. Anal. Calor. 115 (2014) 1949–1960, https://doi.org/10.1007/s10973-013-3372-0.
[88] B. Dong, C. Chen, G. Wei, G. Fang, K. Wu, Y. Wang, Fly ash-based artificial aggregates synthesized through alkali-activated cold-bonded pelletization technology, Constr. Build. Mater. 344 (2022) 128268, https://doi.org/10.1016/j.conbuildmat.2022.128268.
[89] E. L'Hôpital, B. Lothenbach, D.A. Kulik, K. Scrivener, Influence of calcium to silica ratio on aluminium uptake in calcium silicate hydrate, Cem. Concr. Res. 85 (2016) 111–121, https://doi.org/10.1016/j.cemconres.2016.01.014.
[90] X. Pardal, I. Pochard, A. Nonat, Experimental study of Si–Al substitution in calcium-silicate-hydrate (C-S-H) prepared under equilibrium conditions, Cem. Concr. Res. 39 (2009) 637–643, https://doi.org/10.1016/j.cemconres.2009.05.001.
[91] M. Segawa, R. Kurihara, A. Aili, G. Igarashi, I. Maruyama, Shrinkage reduction mechanism of low Ca/Si ratio C-A-S-H in cement pastes containing fly ash, Cem. Concr. Res. 186 (2024) 107683, https://doi.org/10.1016/j.cemconres.2024.107683.
[92] A. Nanakoudis, S.E.M.: Types of Electrons and the Information They Provide, Advancing Materials (2019). ⟨https://www.thermofisher.com/blog/materials/sem-signal-types-electrons-and-the-information-they-provide/⟩ (Accessed 19 February 2025).
[93] S. Joseph, Ö. Cizer, Comparative analysis of heat release, bound water content and compressive strength of alkali-activated slag-fly ash, Front. Mater. 9 (2022), https://doi.org/10.3389/fmats.2022.861283.
[94] A.R. Sakulich, S. Miller, M.W. Barsoum, Chemical and microstructural characterization of 20-month-old alkali-activated slag cements, J. Am. Ceram. Soc. 93 (2010) 1741–1748, https://doi.org/10.1111/j.1551-2916.2010.03611.x.
[95] F. Avet, K. Scrivener, Effect of temperature on the water content of C-A-S-H in plain Portland and blended cements, Cem. Concr. Res. 136 (2020) 106124, https://doi.org/10.1016/j.cemconres.2020.106124.
[96] E. Tajuelo Rodriguez, K. Garbev, D. Merz, L. Black, I.G. Richardson, Thermal stability of C-S-H phases and applicability of Richardson and Groves' and Richardson C-(A)-S-H(I) models to synthetic C-S-H, Cem. Concr. Res. 93 (2017) 45–56, https://doi.org/10.1016/j.cemconres.2016.12.005.
[97] J. Krejsová, R. Kužel, M. Keppert, L. Scheinherrová, A. Vimmrová, New insight into the phase changes of gypsum, Mater. Struct. 57 (2024) 128, https://doi.org/10.1617/s11527-024-02404-z.
[98] V. Viola, M. Catauro, A. D'Amore, P. Perumal, Assessing the carbonation potential of wood ash for CO2 sequestration, Low. Carbon Mater. Green Constr. 2 (2024) 12, https://doi.org/10.1007/s44242-024-00043-9.
[99] E.-J. Moon, Y.C. Choi, Carbon dioxide fixation via accelerated carbonation of cement-based materials: potential for construction materials applications, Constr. Build. Mater. 199 (2019) 676–687, https://doi.org/10.1016/j.conbuildmat.2018.12.078.
[100] A. Król, K. Mizerna, M. Bożym, An assessment of pH-dependent release and mobility of heavy metals from metallurgical slag, J. Hazard. Mater. 384 (2020) 121502, https://doi.org/10.1016/j.jhazmat.2019.121502.
[101] L. Kriskova, V. Ducman, M. Loncnar, A. Tesovnik, G. Žibret, D. Skentzou, C. Georgopoulos, Alkali-activated mineral residues in construction: case studies on bauxite residue and steel slag pavement tiles, Materials 18 (2025) 257, https://doi.org/10.3390/ma18020257.
[102] A. Keulen, A. van Zomeren, J.J. Dijkstra, Leaching of monolithic and granular alkali activated slag-fly ash materials, as a function of the mixture design, Waste Manag. 78 (2018) 497–508, https://doi.org/10.1016/J.WASMAN.2018.06.019.
[103] X. Li, Q. Zhang, B. Yang, Co-precipitation with CaCO3 to remove heavy metals and significantly reduce the moisture content of filter residue, Chemosphere 239 (2020) 124660, https://doi.org/10.1016/j.chemosphere.2019.124660.
[104] Md.A. Taleb, R. Kumar, M.A. Barakat, T. Almeelbi, M.K. Seliem, A. Ahmad, Recent advances in heavy metals uptake by tailored silica-based adsorbents, Sci. Total Environ. 955 (2024) 177093, https://doi.org/10.1016/j.scitotenv.2024.177093.
[105] Y.L. Ni'mah, A.C. Pertiwi, S. Suprapto, Adsorption of Cu(II) on silica gel synthesized from chemical bottle glass waste: Response surface methodology-Box Behnken design optimization, South Afr. J. Chem. Eng. 48 (2024) 55–62, https://doi.org/10.1016/j.sajce.2024.01.007.